Monsoon Planet: Bimodal Rainfall Distribution due to Barrier Structure in Pressure Fields

ANJA KATZENBERGER,[a,b] STEFAN PETRI,[a] GEORG FEULNER,[a,b] AND ANDERS LEVERMANN[a,b,c]

[a] *Potsdam Institute for Climate Impact Research, Member of the Leibniz Association, Potsdam, Germany*
[b] *Institute of Physics and Astronomy, Potsdam University, Potsdam, Germany*
[c] *Lamont-Doherty Earth Observatory, Columbia University, New York, New York*

(Manuscript received 31 January 2023, in final form 4 December 2023, accepted 8 December 2023)

ABSTRACT: Monsoon systems transport water and energy across the globe, making them a central component of the global circulation system. Changes in different forcing parameters have the potential to fundamentally change the monsoon characteristics as indicated in various paleoclimatic records. Here, we use the Atmosphere Model developed at the Geophysical Fluid Dynamics Laboratory (GFDL-AM2) and couple it with a slab ocean in order to analyze the monsoon's sensitivity to changes in different parameters on a planet with idealized topography (varying land position, slab depth, atmospheric CO_2 concentration, solar radiation, sulfate aerosol concentration, and surface albedo). This Monsoon Planet concept of an aquaplanet with a broad zonal land stripe allows us to reduce the influence of topography and to access the relevant meridional monsoon dynamics. In simulations with monsoon dynamics, a bimodal rainfall distribution develops during the monsoon months with one maximum over the tropical ocean and the other one over land. The intensity and extent of the monsoon depend on the relative height of a local maximum in the surface pressure field that is acting as a barrier and is determining the coastward moisture transport. Changes in the barrier height occur during the course of one year but can also be induced when varying different parameters in the sensitivity analysis (e.g., the increase of atmospheric CO_2 reduces the barrier height, resulting in an increase of rainfall, while aerosols have the opposing effect). This bimodal rainfall structure separated by a pressure barrier is also present in reanalysis data of the West African monsoon.

SIGNIFICANCE STATEMENT: Monsoon rainfall directly impacts the livelihood of millions of individuals in the tropics. Because monsoons transport energy and water around the globe, their influence reaches far beyond the tropics, and changes in their dynamics affect the climate both locally and globally. The individual monsoon systems are subject to various forcing factors that determine the monsoon characteristics in partly opposing ways. Here, we implement a model setup of the Monsoon Planet to study the monsoon's sensitivity to various forcings in a simplified design, allowing us to gain new insights into monsoon dynamics. We find that a local maximum in the pressure field is acting as a barrier for moisture transport and thus determines the monsoon characteristics over land.

KEYWORDS: Atmosphere; Atmospheric circulation; Hadley circulation; Pressure; Monsoons; Idealized models

1. Introduction

Monsoon systems can be found in various regions within the tropics and are defined as regions where the prevailing wind directions change at least 120° between the seasons associated with opposite states of humidity, cloudiness, and precipitation regimes (Ramage 1971; Hartmann 2016). Recently, the monsoon concept has been expanded from individually studied monsoon systems toward the concept of a global monsoon (Wang and Ding 2008), strengthening the understanding of the monsoon in the context of the global atmospheric circulation: As large-scale circulation, the monsoon is a central transport mechanism for water and energy across the globe thereby expanding the monsoon's importance toward regions outside the tropics. Therefore, monsoons directly affect the livelihoods of two-thirds of the world's population (Moon and Ha 2020).

The first to propose a scientific theory of the monsoon based on the differential heating of land and ocean was Edmond Halley in 1686 (Halley 1686). His theory was modified in 1735 by George Hadley, who also considered the Coriolis force to be an integral component of monsoon dynamics (Hadley 1735). Further substantial progress has been made particularly since the 1960s (Ding et al. 2015), for example regarding the annual cycle (onset, withdrawal, and active–break cycles), the intraseasonal, interannual, and interdecadal variability, large-scale physical processes, the monsoon's relationship with sea surface temperatures, and the energy and water budget (Ding 2007). Another aspect that was studied in recent decades is the monsoon characteristics under changing anthropogenic driving forces, including the direct effects of greenhouse gas emissions and sulfate aerosols, as well as the indirect effects of changing ocean and land temperatures under global warming (Kitoh et al. 1997; Zhou et al. 2008; Bollasina et al. 2011; Cherchi et al. 2011; Lee and Wang 2014; An et al. 2015; Sarangi et al. 2018; Seth et al. 2019; Wang et al. 2020; Katzenberger et al. 2021,

Supplemental information related to this paper is available at the Journals Online website: https://doi.org/10.1175/JCLI-D-23-0055.s1.

Corresponding author: Anders Levermann, anders.levermann@pik-potsdam.de

DOI: 10.1175/JCLI-D-23-0055.1

2022b; Kripalani et al. 2022; Zhao and Kellogg 1988; Meehl and Washington 1993; Ha et al. 2020; Almazroui et al. 2020; Chen et al. 2020; Moon and Ha 2020). Nevertheless, the mechanisms responsible for monsoon development remain poorly understood (Bordoni and Schneider 2008).

Different methodical approaches are used to gain further understanding of the monsoon's sensitivity to changes in the underlying forcings. Paleoclimatic studies covering the last 252 kyr have revealed that the large-scale meridional temperature gradient and the related position of the intertropical convergence zone shape central monsoon characteristics (Mohtadi et al. 2016; Cai et al. 2015). This temperature gradient is sensitive to various types of forcing, as paleoclimatic evidence in their study shows, including orbital forcing, changes in atmospheric concentration of greenhouse gases, or land-cover changes (Mohtadi et al. 2016; Prell and Kutzbach 1987; Wang et al. 2008).

Another important tool to study Earth's hydrological cycle and its sensitivity to forcings is the concept of aquaplanets (Hess et al. 1993; Smith et al. 2006; Marshall et al. 2007). Such water-covered planet setups are suitable to analyze the annual changes in tropical precipitation following the zenith of the solar insolation: When the ITCZ moves northward (southward) during NH (SH) summer following the seasonal changes in insolation, the Hadley cell and its ascending branch with the corresponding rainfall maximum establishes the characteristic monsoon dynamics northward (southward) of the equator. In addition to this maximum, a second maximum of precipitation evolves during July–September close to the equator in aquaplanet simulations (Lobo and Bordoni 2020; Hui and Bordoni 2021). Nevertheless, aquaplanets omit the role of land and therefore cannot be used to study monsoon rainfall over land.

Therefore, the concept of the aquaplanet was expanded by introducing rectangular-shaped continents, including rectangularly simplified continents, rectangular continents, and land stripes spanning the globe in specific latitudes, in order to study the effect of the land–sea geometry on monsoon circulations (Dirmeyer 1998; Xie and Saiki 1999; Chou et al. 2001; Zhou and Xie 2018; Hui and Bordoni 2021). Xie and Saiki (1999) simplify the form of the Asian continent through rectangular shapes and use a general circulation model to set focus on the abrupt monsoon onset. Another modeling effort using a rectangular tropical continent (30°S–30°N, 0°–45°E) is the Tropical Rain belts with an Annual cycle and a Continent Model Intercomparison Project (TRACMIP), which aims at studying the dynamics of tropical rain belts and their response to past and future radiative forcings (Voigt et al. 2016). Dirmeyer (1998) uses an atmospheric general circulation model and examines the effect of different rectangular land distributions on monsoon rainfall. The focus in that study is on the effect of the latitude of continental coastlines, the meridional and zonal extent of continents, the shape of continents, and the presence of orography on circulation in the tropics and subtropics. The author found that the extension of a subtropical continent into the tropics is critical for establishing heavy convective rainfall over land during the summer season.

A more recent approach has added further insight to this question of which land location is necessary for monsoon dynamics: Hui and Bordoni (2021) use a simplified ESM based on the Geophysical Fluid Dynamics Laboratory's (GFDL) Flexible Modeling System (FMS) to simulate a zonally symmetric continent with an equatorward coastline at 0°, 10°, 20°, 30°, and 40°N and combine it with a slab ocean in order to better understand the seasonal structure of the monsoon, particularly the seasonal transition to an active monsoon state. The "land" is implemented as a hemispheric asymmetry in the mixed layer depth (thus land and ocean only differ by different mixed layer depths of two order of magnitudes). Only in simulations in which the continents extend to tropical latitudes (0°, 10°, 20°N) does the maximum of near-surface moist static energy rapidly transit into the subtropics and with it the ascending branch of the Hadley circulation that can transition into an angular momentum–conserving monsoon regime by allowing internal dynamical feedbacks to operate and shape the response to the smooth insolation into a rapid onset dynamics. Zhou and Xie (2018) set the focus on the hierarchy of various existing setups of idealized monsoon studies by ordering the existing aquaplanet and stripe planet setups by complexity, from aquaplanets over a uniform slab ocean to a subtropical continent that is zonally confined up to a zonally symmetric continent. Besides the monsoon's sensitivity to different land geometry, their study covers the monsoon's response to varying slab ocean depths in an aquaplanet setup, land albedo effects, and the role of ocean heat flux. The particular focus of their study is the basic understanding of the distribution of the surface equivalent potential temperature, which proves to provide a general guide to monsoon rainfall. However, the theory remains diagnostic given that the dynamics determining the distribution is not yet understood (Zhou and Xie 2018). This is in line with Bony et al. (2015), who identified the question of what determines the strength and variability of tropical rainfall as one out of four major challenges in climate science.

In our study, we use an aquaplanet with a zonally symmetric circumglobal land stripe and focus on the land stripe position with an equatorward coastline in the tropics such that the development of monsoon dynamics is possible (Dirmeyer 1998; Zhou and Xie 2018; Hui and Bordoni 2021). Zooming in further compared to previous studies, as much as the 2° latitude grid permits, we find that the clearest monsoon dynamics develop for setups with equatorward coastline locations at 10°N, which overlaps with the approximated coast locations of the most rainfall intense real world monsoon systems. Additionally, we choose the stripe's poleward coastline to be at 60°N inspired by real-world topography. We comprise these setups in the "Monsoon Planet" enabling us to study idealized monsoon dynamics independent of zonal effects. In general, our work complements that of Hui and Bordoni (2021) with some minor differences in the setup. While the study of Hui and Bordoni (2021) uses comparable stripe locations, the underlying model configuration differs in complexity: they use the simplified approach of modeling land as ocean cells with a reduced mixed layer depth. Therefore, land and ocean have the same albedo. Here, we couple our model with the LaD

land module and include a river routing scheme transporting water to the closest ocean cell. In contrast to Hui and Bordoni (2021), land and ocean therefore have a different albedo. In the context of the sensitivity analysis, we also analyze the effect of different land albedo values. In the GFDL-AM2 version that we used for our study, also more complex and realistic physical processes are implemented, such as regarding radiative processes or advection.

While studies with idealized topography have so far mainly focused on the effect of land–sea geometry on the development of monsoon systems, we put the focus of this study on the mechanism of the monsoon development, the possibility of its abrupt emergence, and the sensitivity of the monsoon's rainfall intensity to various forcings, such as changes in carbon dioxide, the solar constant, sulfate aerosols, and surface albedo. To the best of our knowledge, this is the first study bringing together the simplified topographical conditions of an idealized monsoon setup and a comprehensive sensitivity study. For this purpose, we analyze 53 simulations with different Monsoon Planet configurations and one aquaplanet simulation. Our analysis focuses on core monsoon characteristics, such as the Hadley cell expansion, the ITCZ location, the monsoon intensity, and the meridional extent of the monsoon as well as the onset and retreat. A special focus is set on the bimodal distribution of the rainfall distribution that is present in simulations with monsoon rainfall. In this context, it is discussed in which way a local pressure maximum in the coastal area determines the monsoon characteristics.

In section 2, we provide a description of the GFDL-AM2 model and establish the setup of the Monsoon Planet. We also analyze the model's capacity for reproducing monsoon dynamics on real world topography. In section 3, an overview of the general characteristics of the Monsoon Planet setup is given and the role of the moisture–advection feedback is discussed. The local maximum in the surface pressure field that is acting as a moisture barrier and creating a bimodal rainfall distribution is introduced. In section 3, we provide the results of the sensitivity analysis before, finally, discussing the results and concluding in sections 4 and 5.

2. Modeling a Monsoon Planet

a. Model description

We use the atmospheric component GFDL-AM2 of the general circulation model that is developed at the Geophysical Fluid Dynamics Laboratory (GFDL) of the National Oceanic and Atmospheric Administration (NOAA). The main aim in the development process was to create a model with realistic representation of the dynamic, thermodynamic and radiative components of the climate system (Anderson et al. 2004). It solves the primitive equations on the sphere with Earth's radius. A hydrostatic, finite-volume dynamical core is used (Anderson et al. 2004; Delworth et al. 2006). Further information can be found in the supplemental material.

For the horizontal grid a resolution of 2° latitude × 2.5° longitude is used, and quantities are evaluated in a staggered Arakawa B grid (either at the grid center or at the grid corners; Arakawa and Lamb 1977; Anderson et al. 2004). For the vertical grid, a hybrid coordinate grid with 24 vertical levels is implemented. The lowest model level starts about 30 m above the surface and the top level is at about 3 hPa. The vertical resolution is decreasing toward higher altitudes. Advective and physics time steps are 10 min and 0.5 h (Anderson et al. 2004), and for atmospheric radiation 3-h time steps are used in order to include a diurnal cycle (Delworth et al. 2006).

Since the clear focus in this study is on atmospheric processes, we decided to not use a computationally intensive ocean general circulation model but to couple the atmospheric model to a highly simplified "slab-type" ocean model, also referred to as mixed layer model (Knutson 2003; GFDL Team 2019). In this slab ocean module, a horizontal grid of points that represent slabs of water with uniform depth (here 50 m as it is close to the real mixed layer in the ocean) and salinity (33.33 parts per thousand) is implemented. Between the grid points, there is no communication (e.g., no ocean dynamics as currents, temperature advection, diffusion, or convection). Instead, the sea surface temperature at each grid point is the result of the heat exchange across the air–sea and ocean–sea ice interfaces. Corresponding to the use of the slab ocean model, the sea ice model (Winton 2000) is also run in "slab mode."

The implemented land dynamics module LaD (Milly and Shmakin 2002) is based on the early model development of Manabe (1969), who simulates the continents as boxes with limited water storage. In the LaD module, additional physical processes are included as more complex representation of energy (e.g., sensible heat storage) and water storage (snowpack, root-zone water, and groundwater) (Milly and Shmakin 2002). In the land model a rudimentary runoff-routing scheme is implemented. It assumes instantaneous downstream flow of all runoff. Thus, the discharge past any point on a river, at any time, is found as the summation over all upstream cells of the runoff at that time (Milly and Shmakin 2002).

b. Setup of the Monsoon Planet

To focus on the central monsoon characteristics, we idealize Earth's complex topography: Besides simulating the widely studied aquaplanet setup as a reference, we introduce a single circumglobal zonal land stripe ranging from 10° to 60°N and from 180°W to 180°E (Fig. 1a). (The actual latitudinal boundaries differ slightly due to grid resolution.) The equatorward latitude is chosen such that monsoon circulation can evolve in accordance with previous studies (Dirmeyer 1998; Hui and Bordoni 2021). With this design, it is not intended to reproduce any specific individual monsoon, but to create a more general representation of monsoon dynamics comprising the variety of real-world monsoon systems. The northward latitude is derived from real-world topographical conditions and thus it is oriented at the latitudes to which the Arctic Ocean extends. We refer to the simulations by the equatorward coastline (e.g., the 10°N setup refers to the simulation with the land stripe from 10° to 60°N). The stripe design brings the

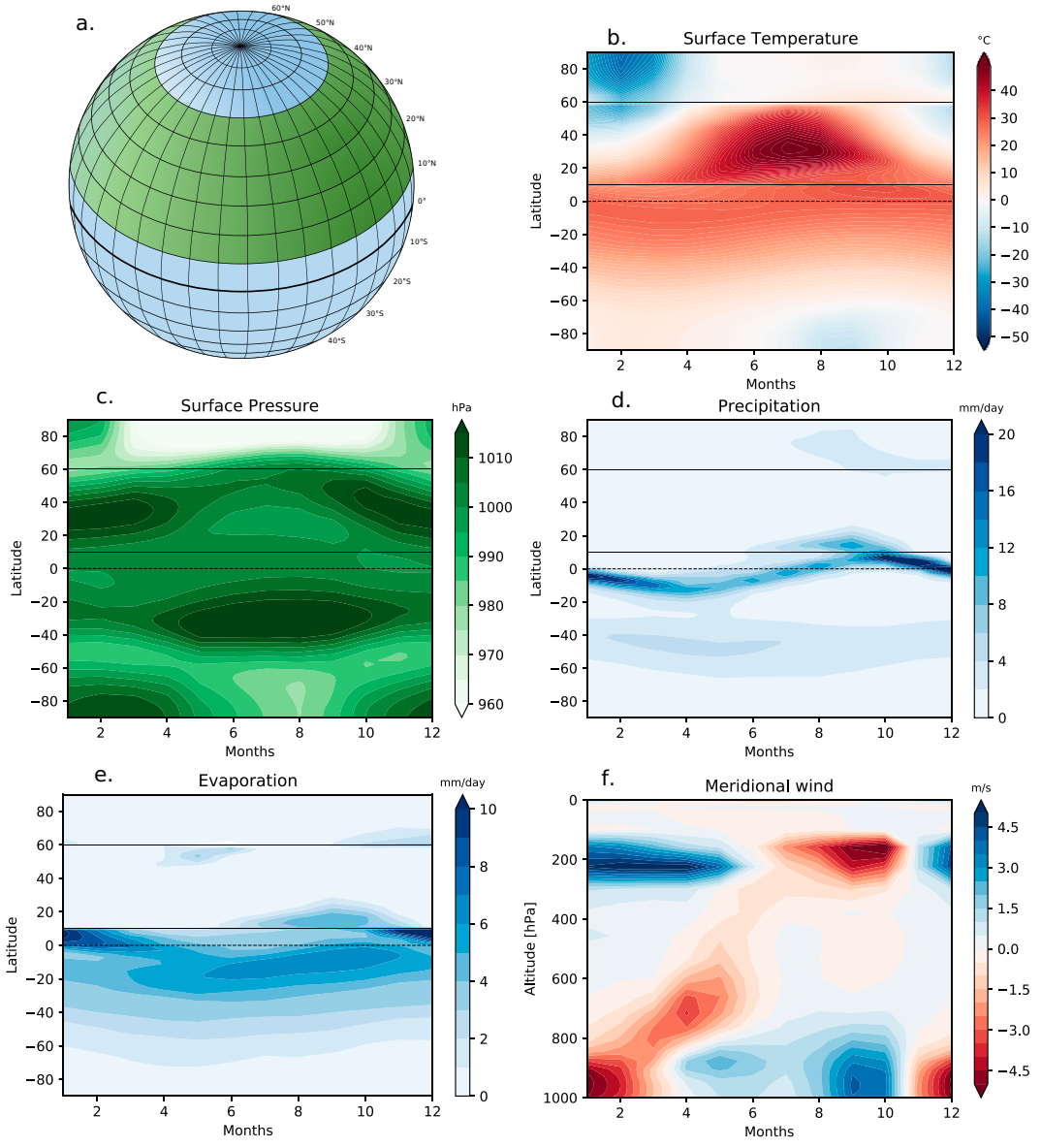

FIG. 1. (a) Conceptual design of the Monsoon Planet with the land stripe at 10°–60°N. The globe-spanning land setup enables us to focus entirely on meridional dynamics, while effects of east or west coasts are omitted. The equatorward coast position is optimal to observe the seasonal precipitation cycle including monsoon rainfall from June to September. (b) Meridional distribution of surface temperature, (c) surface pressure, (d) precipitation, and (e) evaporation for the 10°–60°N configuration at 280 ppm CO_2 during the annual cycle. The horizontal black lines indicate the equatorward and poleward coastlines; the dashed line marks the equator. (f) The annual cycle of the meridional wind (m s^{-1}) for 5°N in the 10°–60°N configuration at 280 ppm CO_2. Positive wind directions refer to winds blowing from south to north.

advantage that there are no zonal effects originated in different topographic east–west conditions, so the analysis can be focused on the meridional dynamics that are central for the monsoon circulation. Placing the landmass on the Southern Hemisphere would provide symmetric results. The orography of these stripes is chosen to be without elevation, and precipitation runoff is routed to the closest ocean cell (i.e., straight northward or southward). The land-cover type chosen is grassland (surface albedo of 18.2%) and land surface roughness is set to 0.

The atmosphere setup is derived from the CM2.1p1 example case in the MOM5 code repository (Griffies et al. 2020; Delworth et al. 2006). Aerosols were excluded. The ozone forcing of the CM2.1p1 example case was globally averaged to global mean values. The concentrations of the greenhouse gases CO_2, CH_4, and N_2O as well as the halocarbons

are set to preindustrial levels. The solar constant is set to 1364 W m^{-2}.

For the sensitivity study, we varied 1) the land position, 2) the slab ocean depth, 3) the solar constant, 4) the carbon dioxide concentration in the atmosphere, 5) sulfate aerosols over land, and 6) the land surface albedo. An overview of the parameter ranges that we applied for simulations are presented in Table 1. For each of the listed setups, GFDL-AM2 was run to provide datasets containing at least 40 years of monthly atmospheric data. The first years were cut off in order to exclude initial stabilization processes, while the remaining 20 years were used to calculate monthly averages. Besides, zonal averages are calculated to access the meridional distributions.

c. *Performance of the model on the present topography*

The performance of the GFDL-AM2 model coupled with a slab ocean and with implemented real-world topography is discussed in the supplemental material in comparison to W5E5 Reanalysis data [over land: WATCH Forcing Data methodology applied to ERA5 data (WFDE5); over ocean: ERA5 (Lange 2019)] with a particular focus on monsoon systems.

3. Monsoons on the Monsoon Planet

a. *General characteristics of the Monsoon Planet*

We use the 10°N setup to explain the general characteristics of the Monsoon Planet, because this configuration reproduces a seasonal cycle comparable to major monsoon systems. The monsoon circulation is driven by changes in the solar insolation throughout the year: The zenith angle of solar insolation is oscillating between 23.5°S (December solstice) and 23.5°N (June solstice). Additionally, the number of hours with daylight varies for different latitudes due to the different orientation of Earth's rotation axis during summer and winter. These two facts determine the incoming solar energy for a given latitude and day of the year (Fig. S3 in the online supplemental material). The surface temperature follows these changes in incoming radiation with a delay, that is larger over ocean than over land reflecting the different thermal properties (Fig. 1b). These land and water properties result also in different surface temperature distributions in the annual cycle: While the region strongly influenced by the incoming solar radiation during NH summer expands up to 60°N over land, over ocean only latitudes up to 30°S are reaching comparable temperatures during SH summer. Also, the cooling effect of rainfall is visible north of the coast after monsoon onset in June.

The surface temperature distribution shapes the formation of high and low pressure systems (Fig. 1c). The low pressure area in low latitudes is what in real-world topography is referred to as the intertropical convergence zone (ITCZ). In the real world as well as in our simulations, the ITCZ expands farther poleward over land compared to the ocean. During the summer months, the warm rising air in the area of maximum surface temperature creates a substantial zone of low pressure over land, while a zone of high pressure over the tropical ocean south of the land forms. The surface pressure distribution translates in meridional surface winds from the high pressure region in the tropical ocean toward land farther north (Fig. 1f).

TABLE 1. Overview of simulations for sensitivity analysis. For a full list of all simulations, see Table S1.

Parameter	Range of variation
Land position	0°–50°, 2°–52°, …, 16°–66°N
Slab ocean depth	50, 200, 500 m
Solar constant	1000–1400 W m^{-2}
Carbon dioxide	70–1120 ppm
Sulfate aerosols (land)	0–10^{-4} kg m^{-2}
Land surface albedo	10%–34%

Arriving over land, the moisture carrying air warms and rises, resulting in convective rainfall. During winter, these winds turn in direction following the opposing pressure pattern. Given these changes in wind direction associated with different rainfall regimes, this precipitation fulfills the defining criteria for monsoon systems. The corresponding rainfall maximum over land (up to 12 mm day^{-1}) is referred to as summer monsoon and reaches up to 25°N. During summer months, a bimodality emerges in the rainfall distribution: The unimodal rainfall maximum begins to reveal a splitting tendency in April that results in a clear bimodal rainfall distribution between June and September (Fig. 1d). One peak of the rainfall distribution is located over land, while the other rainfall maximum is located over the tropical ocean. Further details of the bimodality are discussed in section 3b. The average global annual rainfall in the standard simulation is 946.4 mm and the average annual rainfall in the monsoon region (10°–30°N) is 510.6 mm. The spatial distribution of the rainfall including the zonal dimension is presented in Fig. S4.

The global mean temperature is 16.8°C. From November to June, there is sea ice on the polar regions of the NH extending up to 60°N, while from July to November there is sea ice on the SH extending also up to 60°S. The north of the land stripe (50°–60°N) is seasonally covered with snow from October to April. In the supplemental material, further information as, for example, regarding the monthly meridional distribution of precipitation minus evaporation (Fig. S5) and the mass streamfunction for the monsoon months (Fig S6) is given.

b. *The bimodal rainfall distribution*

In configurations with a land stripe sufficiently far south (e.g., 10°–60°N), the rainfall distribution exhibits a bimodal spatial distribution during the monsoon season (Fig. 2). The surface pressure field can explain how this bimodality develops (Fig. 3): In January, the surface pressure minimum is located at 5°S following the incoming solar radiation and the resulting surface temperatures. South of 5°S, the surface winds follow the gradient of the pressure distribution toward the north, while north of 5°S the winds flow southward. At the pressure minimum, these winds with opposing direction meet forming a zone with uprising air mass that is associated with

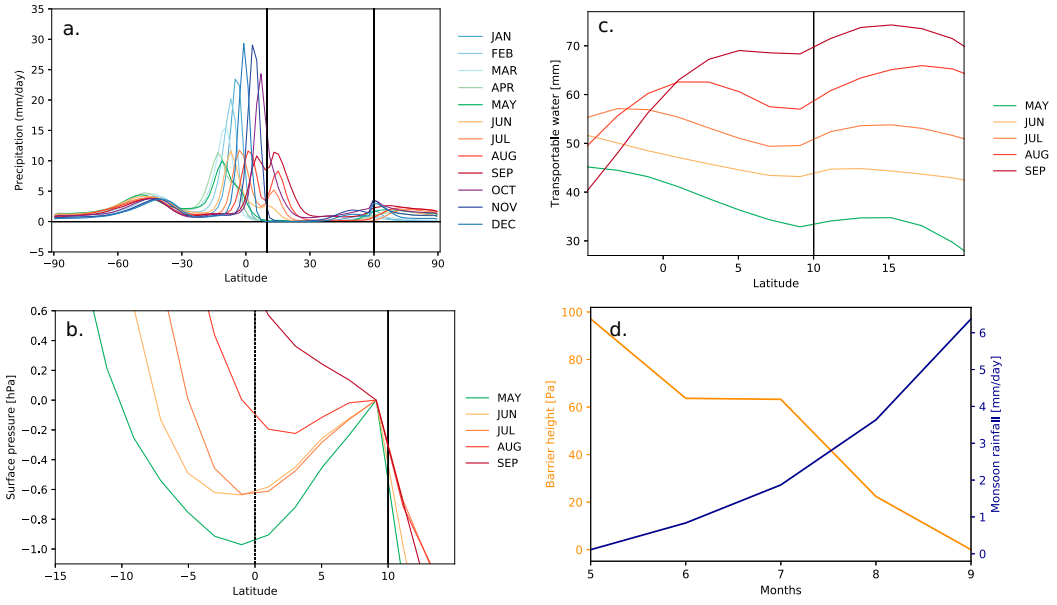

FIG. 2. (a) Meridional rainfall distribution for the months of the year. A bimodal structure becomes visible during the monsoon season. (b) Meridional distribution of surface pressure from 15°S to 15°N for May–September minus surface pressure at the grid cell 9°N. The local maximum at the coast acts as a pressure barrier for the moisture transport toward land. Its relative height decreases from May to September, analogously to the increase in monsoon rainfall. It must be noted that the different effects of land and ocean seem to be visible at 9°N, while actually land starts at 10°N. This is due to the fact that the quantities are evaluated at the center of a grid cell (here approximately 9° and 11°N), while land starts at the boundaries of the grid cells. (c) Transportable water (water vapor column) for 5°S–20°N for May–September. (d) Relative height of surface pressure barrier and monsoon rainfall for the months May–September.

convective rainfall. In February, the dynamics is the same only a few degrees farther north. In March, the area around the equatorward coast receives enough solar radiation such that a relative difference between land and ocean becomes visible in the surface pressure distribution: While the land close to the coast warms relatively fast, the ocean close to the coast warms comparatively less with the same level of incoming solar radiation. While the relatively high temperatures over land create rising air movement associated with a local pressure minimum, the temperature over the ocean does not change enough to create relevant changes in the surface pressure compared to the distribution in the previous month. Thus, the surface pressure level over the ocean remains at a specific level, while in the adjacent land cells the pressure is decreasing. This leads to the creation of a local maximum over the ocean, and a local minimum over land. The structure of a relative pressure barrier (difference between this local maximum and local minimum in the surface pressure distribution) is created. While the sun is moving farther north during the course of the year, the low pressure zone moves farther north and becomes more pronounced. The pressure maximum acts as a pressure barrier preventing strong moisture carrying winds from flowing farther north also in April and May. As a consequence, there is no moisture transport from the ocean to the land and very little rain. During the next months, the relative height of the pressure barrier decreases (Fig. 2b), allowing moisture carrying winds to pass. As the pressure barrier decreases, more and more moisture reaches the land. Arriving at the warmer land, these air masses rise and create convective rainfall, resulting in a second rainfall maximum over land (Fig. 2c). The bimodal structure emerges (Fig. 2a). The relative height of the pressure barrier decreases only slightly between June and July, while the monsoon rainfall differs relevantly (Fig. 2d). This shows that after the monsoon onset, the amount of available water in the regions that provide for the monsoon rainfall are also playing a relevant role for determining the amount of monsoon rainfall. As the solar radiation moves the pressure distribution toward south later in the season, the two pressure minima grow together reuniting the bimodal rainfall distribution. The rainfall over land cools the surface temperature, leading to an increase in surface pressure, which modulates the form of the pressure distribution. Nevertheless, the influence on the pressure distribution is comparatively minor.

This bimodal rainfall distribution is a central characteristic of idealized monsoon systems. It occurs not only during the course of one year, but can also be observed by varying different parameters and therefore changing the surface pressure distribution and the relative height of the pressure barrier. The details of this dynamics will be analyzed in the following sensitivity study.

The bimodal structure in the rainfall distribution is also present in W5E5 reanalysis data covering the West African

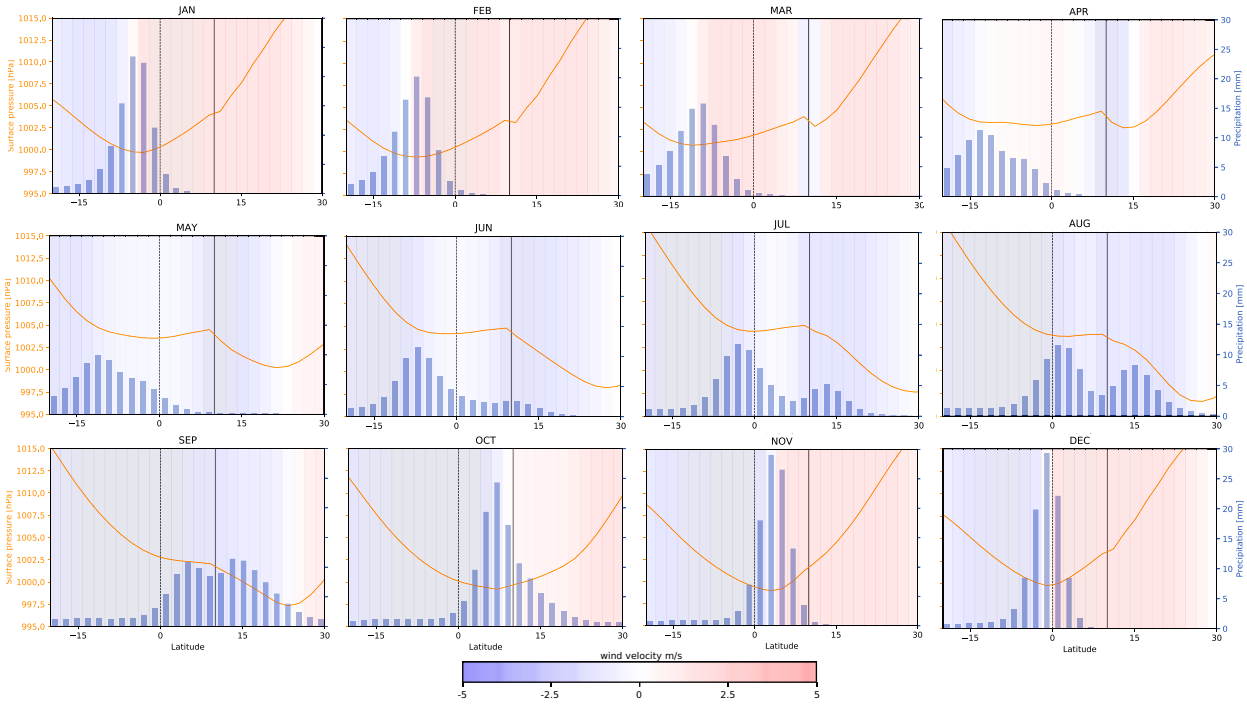

FIG. 3. Development of bimodal rainfall structure (blue bars) dependent on pressure distribution (orange lines) and resulting wind directions (background colors). Red background colors indicate north wind, blue background color south winds. The intensity of the background color refers to the wind velocity.

monsoon (5°–15°E) where the topographic conditions are relatively similar to the stripe setup of the Monsoon Planet with equatorward coast at 4°N (Fig. 4). During the monsoon season from June to August, the northward rainfall maximum increases and the bimodality intensifies. In September, the retreat of the monsoon is visible as a decrease of the northward maximum. The location of the two rainfall maxima are determined by a pressure barrier. It varies only slightly in its relative height during the monsoon season indicating a relevant role of the moisture availability in the moisture supplying areas. Besides, the location of the maxima differs between the reanalysis data and the idealized study.

c. *Energy budget on the Monsoon Planet*

The major components of the energy budget for an atmospheric column in the monsoon region between 10° and 30°N are sensible heat, latent heat release induced by precipitation, radiation, and convergence. Figure 5 shows the annual cycle of the energy budget for the 10°–60°N setup and an aquaplanet setup. On an aquaplanet the beginning of spring brings the same change in solar insolation as on Earth to the tropical region between 10° and 30°N. This additional energy is, however, absorbed by the ocean. Due to the large heat capacity of water compared to soil this does not lead to a significant temperature increase near the surface. By contrast, if the region between 10° and 30°N is occupied by land, the additional solar

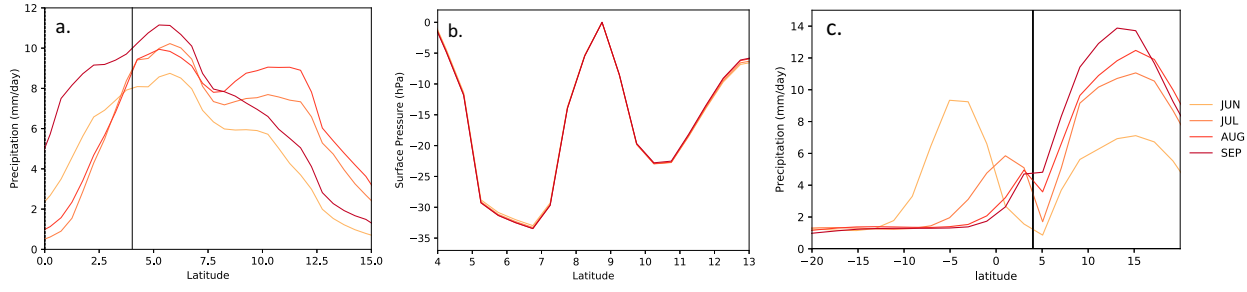

FIG. 4. (a) Meridional precipitation and (b) surface pressure distribution from 4° to 13°N over the West African monsoon area for June–September minus pressure at the grid cell at 9°N. The continuous line indicates the approximate southern latitude of the West African coast. (c) For comparison, the meridional precipitation on the Monsoon Planet with a land stripe starting at 4°N is given.

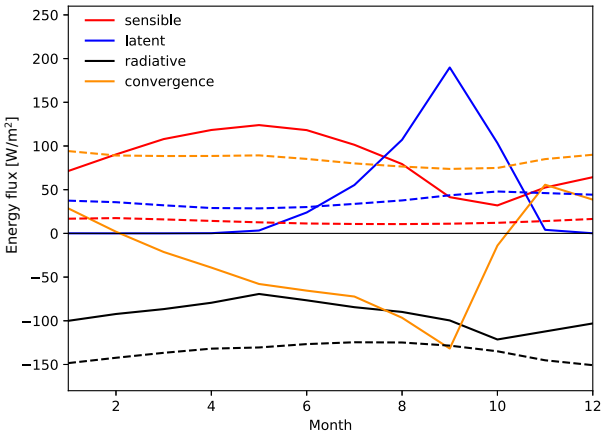

FIG. 5. Energy budget during one annual cycle for the 10°–60°N setup (continuous lines) and the aquaplanet setup (dashed lines). The data for this figure are extracted from the atmospheric column over the monsoon region from 10° to 30°N. The different components are sensible heat (red), latent heat release induced by the precipitation (blue), radiation (black), and inferred convergence (orange).

insolation yields a temperature increase of the land. This can be seen from the energetic response, which is an increase of sensible heat from the land to the atmosphere. At the height of this sensible heat flux in May rain starts to fall. This is due to the rising air masses over land that are induced by the surface temperature increase. As a response to the rainfall the temperature of the land declines and with it the sensible heat flux. The release of latent heat due to the rainfall however warms the atmospheric column and sustains a temperature difference between the land and the ocean. This temperature difference yields an ageostrophic wind carrying moist air from the ocean toward the land as can be seen from the increase of net advective energy transport toward land. The cycle including the release of latent heat constitutes a self-sustaining (positive) feedback loop as described in Levermann et al. (2009).

4. Monsoon's sensitivity to physical factors

The baseline run with the land stripe from 10° to 60°N described in section 3a is modified by varying various forcing parameters. The following sections describe the results of this sensitivity analysis with particular focus on the role of the pressure barrier acting as a blocking structure for moisture transport toward land. In addition, monsoon intensity, extent, and length of the season are analyzed. Furthermore, insights into the ITCZ location and the Hadley cell are provided.

a. Sensitivity to the land position

To understand which land positions allow monsoon dynamics to develop and how different land positions influence the monsoon characteristics, we move the land stripe from 16° to 66°N in steps of 2°N farther southward until 0°–50°N. The stripe width is always 50°, but it is important to keep in mind here that therefore the area covered by land differs in the different setups given the spherical shape of the planet. By varying the land location, the according lower heat capacity compared to the ocean as well as the different albedo is distributed differently over the latitudes in the NH changing the radiative budget. The meridional precipitation for selected runs is shown in Fig. 6, and for all other simulations in Fig. S7.

By comparing the monsoon rainfall on different land positions (from the equatorward coast to 30°N) to the aquaplanet (at the same latitudes), the configurations can be ordered in three classifications based on their dominant behavior. Figure 7a shows the annual monsoon rainfall in the monsoon area, which we define to be between the equatorward coast and 30°N independent of the different stripe positions. The upper latitude threshold is chosen because in all stripe locations the monsoon rainfall over land takes place south of 30°N. Given this definition, the corresponding area increases when the stripe is moved farther equatorward. This effect combined with the increasing consequent overlap with the convergence zone results in an increase of monsoon rainfall when the stripe is placed farther equatorward. When this is compared to the rainfall distribution within the same latitudes on the aquaplanet, the effect of the presence of land in certain latitudes becomes accessible: The 16°, 14°, and 12°N setups show the effect of pushing the rainfall distribution away farther south and are therefore classified as the "monsoon repellent" setups. The 12°N setup is dominated by this repellent behavior, but already shows weak dynamics of monsoon rainfall. The 10°, 8°, 6°, 4°, and 2°N setups enable the development of monsoon rainfall over land. They attract additional rainfall compared to the reference rainfall on the aquaplanet. This additional rainfall is a result of the bimodal rainfall distribution and one of the two rainfall maxima that are placed over land (see also section 3b). The second maximum is located south of the land stripe in the tropical ocean. We classify these setups as bimodal monsoon systems. The 0°N also fulfills the monsoon definition of seasonal changing wind directions associated with different states of rainfall, but this simulation is dominated by a unimodal behavior during the monsoon months identifying this run as a unimodal monsoon system.

On the aquaplanet setup without a land stripe, the zonal averaged precipitation shows a clear central maximum around the equator that varies following the maximum of the solar radiation during the seasons, with rainfall reaching up to 12°N in the NH and 12°S in the SH (Fig. 6). This precipitation can be interpreted as monsoon rainfall since for a given location, the amount of rainfall as well as the wind direction vary between the seasons, which is the definition of a monsoon. This rainfall maximum indicates the area of convective rainfall in the rising branch of the Hadley cell. While there are a variety of indices available in the literature in order to calculate the position of the ITCZ, we use here the maximum of the zonally averaged precipitation minus evaporation (Johanson and Fu 2009). The upper and lower edges of the Hadley cell have been derived using the outgoing longwave radiation: The subsidence regions of the Hadley circulation can be identified as the regions with high outgoing longwave radiation because of their dry troposphere and the lack of high clouds. Thus, the maximum poleward expansion of the Hadley circulation is defined as the most poleward latitude where the zonal-mean outgoing longwave radiation equals 250 W m^{-2}(Hu and Fu 2007). The Hadley cells in the aquaplanet reach up to 30°N

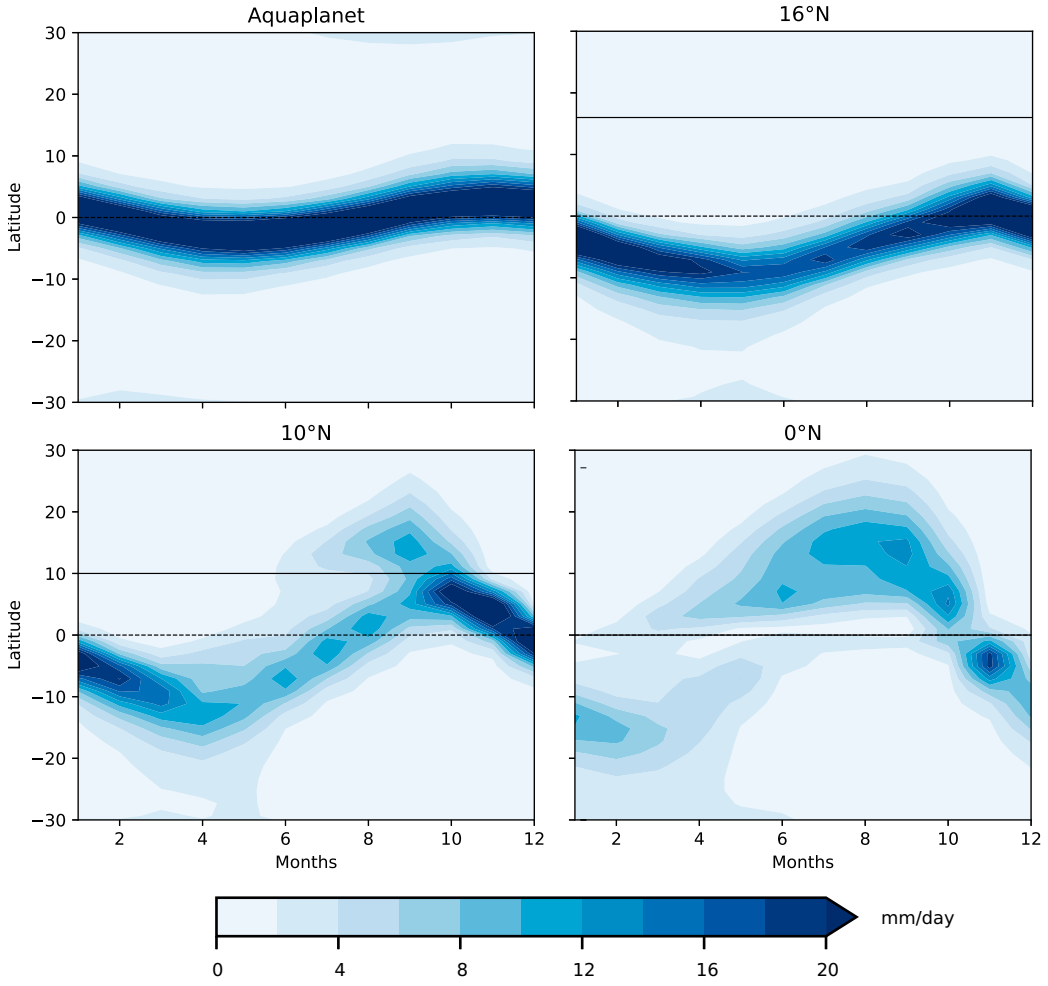

FIG. 6. Meridional distribution of precipitation for the aquaplanet and Monsoon Planet with different stripe positions during the annual cycle. The horizontal black line indicates the equatorward coastline, and the dashed line marks the equator. The precipitation for the other stripe positions is shown in Fig. S7.

(30°S). Accordingly, the subsidence zone of the Hadley zone is within the dry area south (north) of 30°N (30°S). Besides, two secondary maxima develop in the middle latitudes at approximately 40°S and 40°N where extratropical cyclones are frequent; see also Manabe (2019).

When an idealized continent is introduced between 16° and 66°N, land is too far from the ITCZ for the emergence of monsoon rainfall over land. In these configurations the land is basically pushing the rainfall away toward more southern latitudes by means of the pressure minimum over land and the resulting local pressure maximum near the coast. While the seasonal path of the precipitation remains, it is shifted approximately 5° southward (Fig. 6). This shift coincides with a southward shift in latitudes where north and south winds meet and form rising motion and corresponding convective rainfall (Fig. 8a). Given that these meridional surface winds follow the surface pressure, the surface pressure has a minimum at these latitudes. On the aquaplanet setup this minimum is in the area of the equator during NH summer, while in the 16°N setup it is farther south. The different location of the surface pressure minimum originates in the development of an additional local minimum over land and correspondingly a new local maximum over the south coast of the land in the 16°N setup, shifting the local minimum farther south (Figs. 8b,c).

While the expansion of the Hadley cell on the SH is not changed compared to the aquaplanet setup, the Hadley cell on the NH expands farther over land during summer (Fig. 8a). This is a result of the land stripe warming faster (than the water that exists in this area in the aquaplanet setup), creating zones of rising air, and accordingly shifting the subsidence zone farther northward. Additionally, the secondary maximum on the NH is strongly suppressed by the presence of land and a strong reduction of evaporation.

Placing the land 2° farther south at 14°–54°N, the effect of the land pushing the rainfall southward remains but is weaker with an average southward shift of 3°N. The shift compared to the aquaplanet is strongest during the first half of the year,

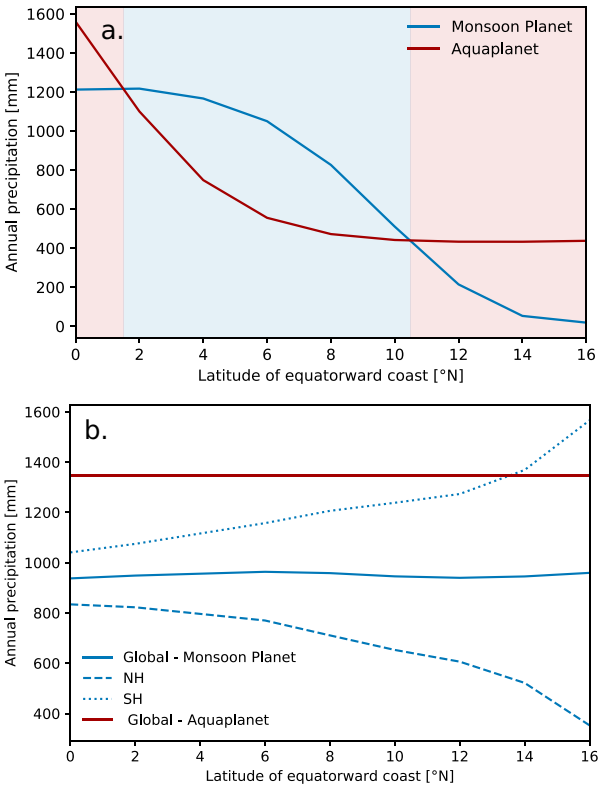

FIG. 7. (a) Annual precipitation in the area from the latitude of the equatorward coast to 30°N for the aquaplanet (red) and Monsoon Planet (blue). (b) Dependence of annual rainfall over the globe and the Northern and Southern Hemispheres on the location of the south coast of the land stripe. The global precipitation (blue) is relatively constant. While the rainfall on the Northern Hemisphere decreases when the land stripe is moved south, the rainfall on the Southern Hemisphere increases. As a reference, the global precipitation on the aquaplanet experiment is also indicated (red).

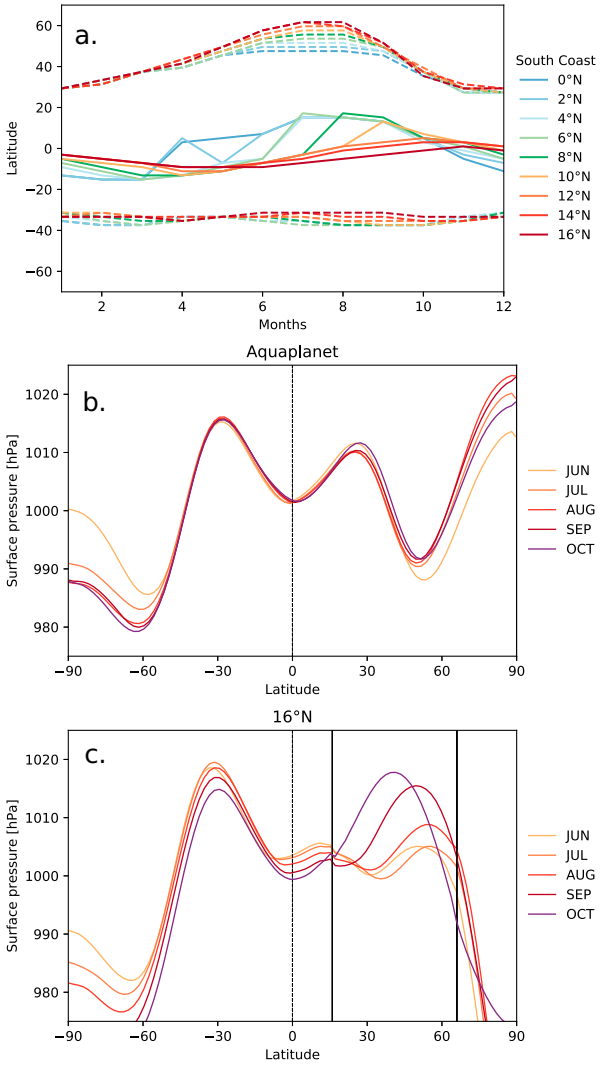

FIG. 8. (a) Seasonal changes in the northward extension of the Hadley cell (dashed upper lines), the location of the ITCZ (middle lines), and the southward extension (dashed lower lines) for the Monsoon Planet configurations with varying latitudes of the equatorward coast and the aquaplanet setup. The location of the ITCZ has been calculated as the maximum of precipitation minus evaporation (Johanson and Fu 2009). The upper and lower edges of the Hadley cell have been derived using the outgoing longwave radiation: The subsidence regions of the Hadley circulation can be identified as the regions with high outgoing longwave radiation because of their dry troposphere and the lack of high clouds. Thus, the maximum poleward expansion of the Hadley circulation is defined as the most poleward latitudes where the zonal-mean outgoing longwave radiation equals 250 W m^{-2} (Hu and Fu 2007). Also shown is the meridional distribution of surface pressure for the (b) aquaplanet configuration at 280 ppm CO_2 and (c) 16–66°N Monsoon Planet setup during the annual cycle. The horizontal black line indicates the equatorward coastline, and the dashed line marks the equator.

whereas it vanishes from August to November. The Hadley cell is located comparable to the 16°N run (Fig. 8a). In September and October, there is some very weak rain directly at the coast but the land stripe is still too far for a relevant monsoon dynamic to develop (Fig. S7).

When the equatorward coastline is placed at 12°N, weak monsoon rainfall over land begins in August and retreats in October (Fig. S7). The closer the south coastline is to the equator, the earlier the rainfall maximum "jumps" over to the land stripe, leading to an earlier monsoon onset and a later retreat (Fig. 8a and Fig. S8). This is not only an effect of the land being close enough to the equator that the seasonal rainfall maximum path overlaps with land in this setting, but also a bimodal structure of the rainfall distribution developing and strengthening rainfall in the coastal area. If the land stripe is moved farther south to 10°N, the bimodal split becomes even more dominant (see also section 3b). The bimodal split can also be observed for the 8°, 6°, 4°, and 2°N setup, but is converging more and more to a unimodal rainfall distribution during the monsoon months when moving the land stripe farther south.

In the 0° setup, there is basically no bimodal behavior (Fig. 6). Instead, the rainfall "arm" over land has become the major unimodal distribution. The monsoon rainfall over land begins even earlier given the proximity to the equator and therefore the monsoon trough. The rainfall amount over land is higher than the rainfall over ocean, revealing asymmetric behavior. This is a result of the NH with land warming faster than the SH with ocean, leading to moist monsoon winds toward the north during more than half of the year.

Compared to the global precipitation on the aquaplanet of 1348 mm, there is less rainfall on setups including land (Fig. 7b). This is caused by the fact that the evaporation is strongly reduced over the land area. The global precipitation in setups with different land distribution is relatively constant (approximately 950 mm). Nevertheless, the rainfall distribution to the two hemispheres changes: while the rainfall on the Northern Hemisphere is decreasing when the land stripe is moved southward, the rainfall on the Southern Hemisphere is increasing. This fits with the fact that the area covered by land increases when the land stripe is moved farther southward (the land stripe of 50° does not have the same area everywhere on the globe) suppressing more evaporation. The suppressed rainfall amount adds on top of the rainfall of the SH creating symmetric changes in rainfall. This is a result of the pressure barrier reducing in height for land positions closer to the equator regulating the moisture transport toward land. Interestingly, the global mean surface temperature is for all land stripe locations between 17° and 18°C. The effect that land warms faster during the summer months is balanced by the faster cooling during winter months.

b. *Sensitivity to slab ocean depths*

The depth of the mixed layer slab ocean determines the ocean's heat capacity. While the water mass of a relatively deep ocean needs more time to warm up, shallow water reaches thermal equilibrium with the incoming solar radiation on a much shorter time scale. We refer to the setup with a slab ocean depth of 50 m as slab50 and analogously for depths of 200 and 500 m.

As the zenith angle oscillates between 23.5°S and 23.5°N, the sea surface temperature of slab50 follows the solar zenith angle by warming and cooling relatively fast, while a deeper slab ocean of 200 or 500 m stores the heat symmetrically around the equator with weaker seasonal variation (Fig. 9). The different extent of the seasonal variation of the sea surface temperature in the different slab ocean depth setups translates also into the different latitudinal extension in the seasonal variation of the ITCZ and the according convective rainfall (Fig. S9 and Fig. 9). Given this stronger meridional oscillation of the rainfall trough in the simulations in slab50, the rainfall trough reaches much closer to land in this simulation. This appears to enable the rainfall to "jump over" to the land, supporting the development of stronger monsoon dynamics in slab50 compared to slab500, including a further spatial monsoon extension toward the north, a higher rainfall intensity (Fig. 9), and a longer monsoon season with earlier onset and later retreat (Fig. S10). Regarding the monsoon

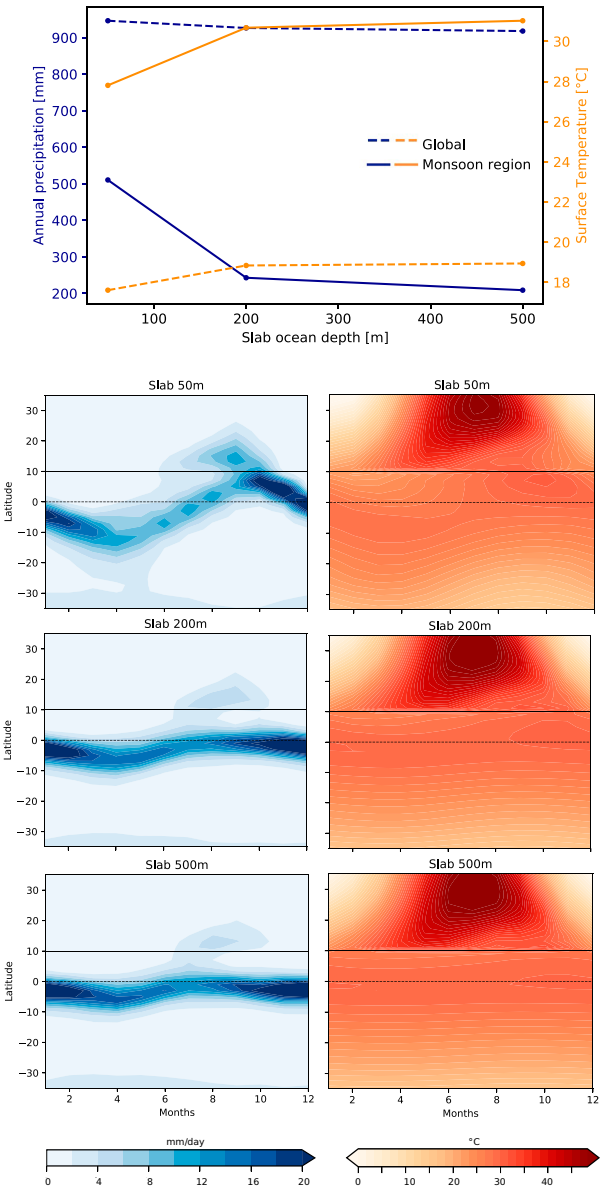

FIG. 9. (top) Sensitivity of precipitation and surface temperature to changes in the slab ocean depth. The continuous lines refer to the relationship in the monsoon region (10°–30°N), while the dashed lines indicate global relationship. (bottom) Rainfall and surface temperature distribution for each month for the 10°N stripe configuration with different slab ocean depths (50, 200, 500 m). The horizontal black line indicates the equatorward coastline position, and the dashed black line marks the equator. The slab50 simulation is the same as the standard run. Slab200 and slab500 are based on the standard run but vary in the slab ocean depth.

extension, the monsoon affected land region (>2 mm day^{-1}) expands farther northward in slab50 (27°N) compared to slab200 (21°N) and slab500 (20°N).

The reason for the more pronounced monsoon characteristics in slab50 compared to slab500 is based on the dynamics in

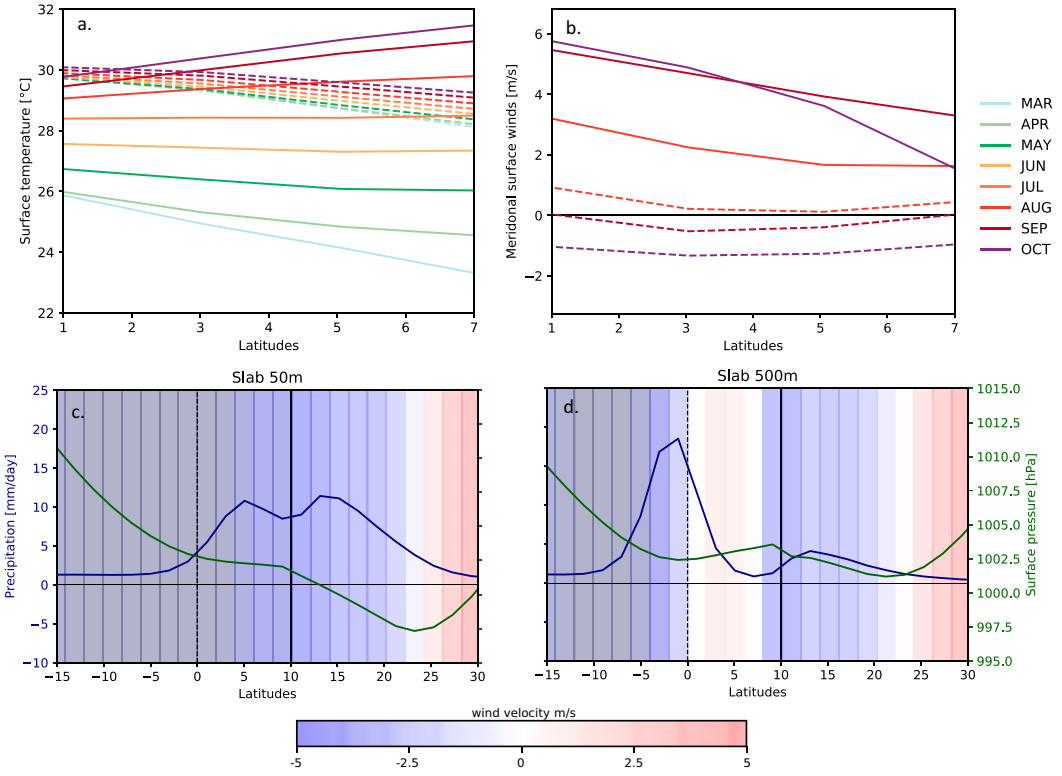

FIG. 10. Surface temperature distribution for each month for the 10°N stripe configuration with different slab ocean depths for (a) slab50 and (b) slab500. The horizontal black line indicates the equatorward coastline position, and the dashed black line marks the equator. (c),(d) Meridional precipitation and surface pressure distribution for September. The background colors refer to the meridional surface wind velocity. Red regions refer to north winds, while blue regions indicate south winds. The more intense the color, the higher the wind velocity.

the area between the equator and the coastline at 10°N: Between March and October, the insolation conditions lead to a warming in this latitude zone, stronger in 5°–10°N compared to 0°–5°N. Given the different heat capacities of the 50 and 500 m configuration, the north of this zone warms up relatively fast in slab50, while the change in slab500 is on a much smaller scale (Fig. 10a). As a result, the surface pressure minimum is located more north in slab50 compared to slab500. The subsequent pressure gradient leads to northward winds in slab50 and southward winds in slab500 in the region from 0° to 10°N (Fig. 10b). Accordingly, the moisture that the air receives via evaporation in this ocean zone is transported northward in slab50 and southward in slab500. Therefore, these moisture carrying winds contribute to the monsoon rainfall over land in slab50, while it contributes to the rainfall maximum over ocean in slab500. This leads to different meridional rainfall distributions including stronger monsoon rainfall over land. Figures 10c and 10d show the situation exemplary for September.

Besides, we identified the expansion of the Hadley cell by using the outgoing longwave radiation as explained in the previous subsection following the method of Hu and Fu (2007). While there is little seasonal movement for the southward edge of the Hadley cell, a strong variation can be seen in the northward edge. This is a result of the different thermodynamic properties of land and ocean (Fig. S9). Over ocean, the southward edge is expanding slightly more south in the 50 m configuration compared to the 500 m configuration due to the different heat storing capacities.

c. *Sensitivity to solar constant*

Changing the solar radiation (increasing the incoming shortwave radiation) determines the radiative forcing. Stronger radiative forcing results in higher global mean temperatures. This also shapes the water cycle given, for example, the enhanced evaporation or the resulting warmer atmosphere that is capable of holding more moisture following the Clausius–Clapeyron relation. Accordingly, the global precipitation patterns are changing. Here, we vary the total globally incoming solar radiation from 1000 to 1400 W m^{-2} in order to understand the effect of varying solar radiation on monsoon characteristics on a planet with idealized topography.

Changes in the solar constant lead to changes in the global mean temperature. The global mean temperature is 26.4°C for 1400 W m^{-2}, 17.3°C for 1300 W m^{-2}, and 6.3°C for 1200 W m^{-2}. Figure 11a shows the resulting surface temperature distribution for three setups. This figure also indicates the dependence of the

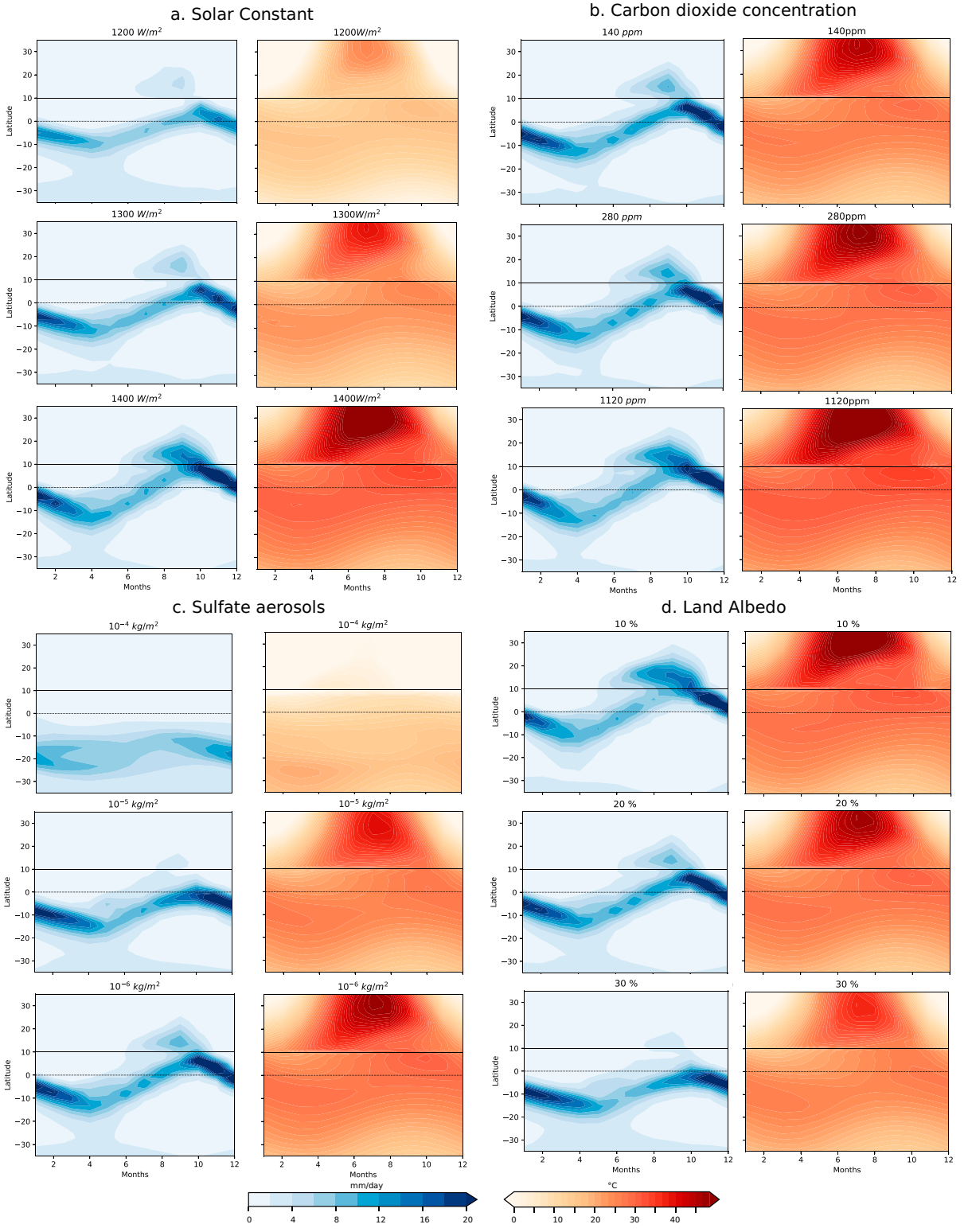

FIG. 11. Meridional distribution of precipitation and surface temperature during one year for different values of the (a) solar constant, (b) carbon dioxide concentration, (c) sulfate aerosol concentration, and (d) land albedo. The horizontal line indicates the location of the land stripe. The dashed line marks the equator.

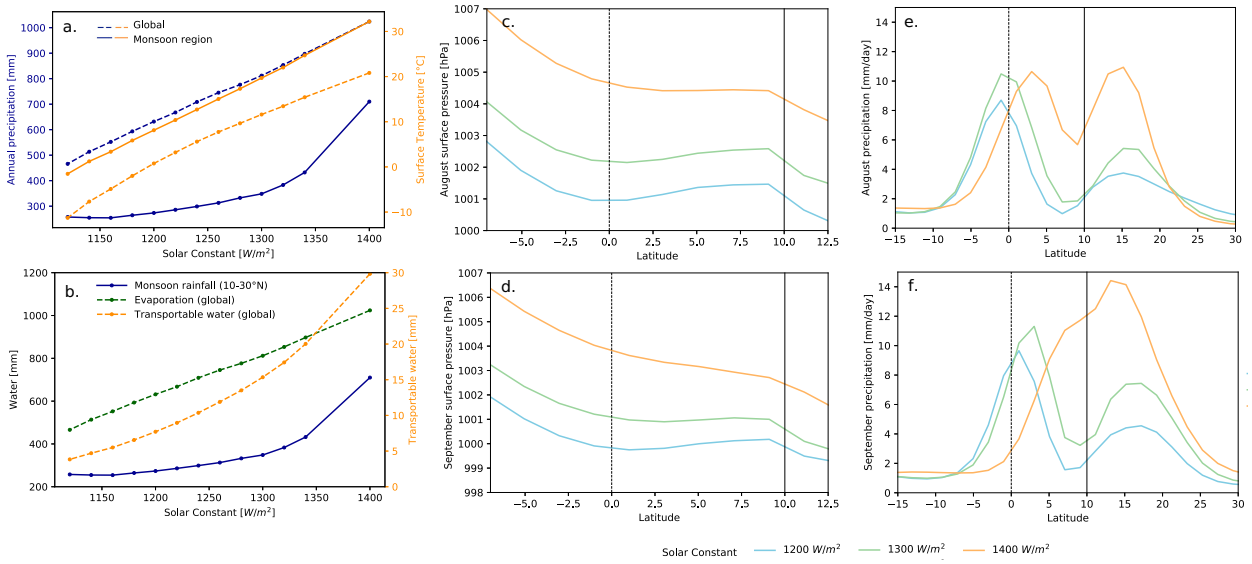

FIG. 12. (a) Sensitivity of precipitation and surface temperature to changes in the solar constant. The continuous lines refer to the relationship in the monsoon region (10°–30°N), while the dashed lines indicate the global relationship. (b) Annual rainfall in the monsoon region from 10° to 30°N dependent on different values of the solar constant (blue). Also, the contribution from evaporation in 90°S–10°N and 10°–30°N is given (green). The water vapor content (orange) shows the increasing moisture content in the atmosphere. Only the nonfrozen configurations are shown. (c)–(f) Meridional distribution of surface pressure and precipitation for selected solar constant values and for August and September. The dashed line marks the equator, and the continuous line indicates the beginning of land. For details regarding the offset between the beginning of land and the visible difference between land and ocean refer to Fig. 2.

global surface temperature on the solar constant. If the solar constant is below 1080 W m^{-2}, the planet is completely frozen and no relevant monsoon rainfall is remaining. Already in the simulation with 1100 W m^{-2}, the pre-tipping dynamic is visible as strong variability (Fig. S11).

As a result of the increase in global surface temperatures, global precipitation increases (Fig. 12a). This global increase of precipitation is not distributed uniformly across the globe, but is in comparison stronger in the monsoon area in 10°–30°N, particularly in the region from 20° to 30°N. This local and global increase in precipitation originates in the increase in sea surface temperature and thus, an approximately linear increase of evaporation over the ocean. Additionally, the water vapor content of the atmosphere is increasing nonlinearly following the Clausius–Clapeyron relation (Fig. 12b).

The increase of monsoon rainfall is associated with a farther northward expansion over land: While the monsoon in the 1200 W m^{-2} setup reaches up to 24°N, it reaches 26°N in the 1300 W m^{-2} setup and 28°N in the 1400 W m^{-2} setup. The maximal extension is during September for all setups. The increase of the spatial extension is related to the higher surface temperatures over land that enables rising air motion farther north. This coincides with the observation that the Hadley cell expands farther north and south (Fig. S12). Besides, the amplitude of the seasonal variation of the ITCZ increases. The monsoon intensity increases during June–November, but the monsoon season is only prolonged slightly (Fig. S13).

Changes in the incoming solar radiation also shape the relative height of the surface pressure barrier at the coast: While the pressure barrier has a relative height of 51 Pa for 1200 W m^{-2} in August, it reduces to 44 Pa for 1300 W m^{-2} and 30 Pa for 1400 W m^{-2}. Regulated by the relative height of the pressure barrier, the monsoon rainfall increases from simulations with low solar constant values to high values. Thus, the rainfall maximum around the equator is dominating in the 1200 and 1300 W m^{-2} setup, but in the 1400 W m^{-2} setup the maximum at the equator and at 15°N are of similar height (Figs. 12c,e). Comparable dynamics are occurring in September. For the 1400 W m^{-2} simulation, the pressure barrier vanishes entirely enabling strong moisture transport and allowing the two maxima to unite to a unimodal rainfall distribution (Figs. 12d,f).

d. Sensitivity to the carbon dioxide forcing

Here, we vary the carbon dioxide concentration from 70 to 1120 ppm, including the preindustrial as well as the current carbon dioxide concentration. A higher concentration of atmospheric CO_2 leads to increased surface temperature and accordingly increased global mean temperature (Fig. 13a). This leads to globally increased evaporation on the one hand and more water vapor in the atmosphere on the other hand (Fig. 13b). As a consequence, this enables greater scales of horizontal transport of water vapor by the large-scale circulation. These thermodynamically induced changes in the hydrological cycle strengthen the tropical rainfall, particularly in the monsoon region (Fig. 11b). The monsoon rainfall in dependence of the surface temperature behaves relatively independently of the origin of the surface temperature change (solar constant or the atmospheric carbon dioxide; see Fig. S14). For the 140 ppm setup, the monsoon extents up to 25°N, for the 280 ppm setup up to 26°N, for the 560 ppm setup up to 27°N,

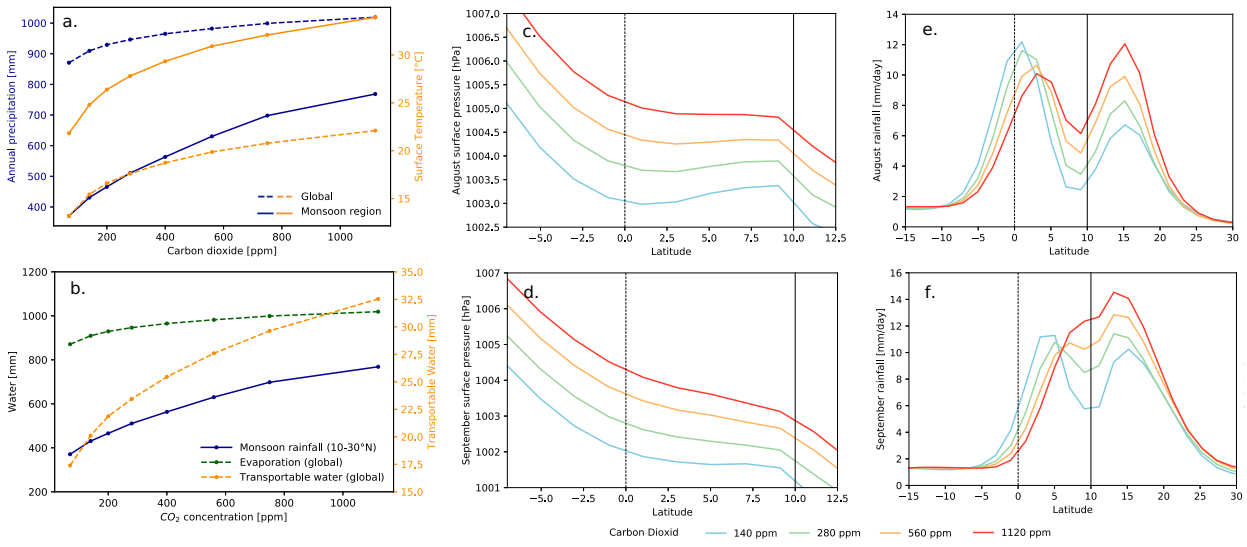

FIG. 13. (a) Sensitivity of precipitation and surface temperature to changes in the atmospheric carbon dioxide concentration. The continuous lines refer to the relationship in the monsoon region (10°–30°N), while the dashed lines indicate the global relationship. (b) Annual rainfall in the monsoon region from 10° to 30°N dependent on different values of the solar constant (blue). Also, the contribution from global evaporation is given (green). The water vapor content (orange) shows the increasing moisture content in the atmosphere. (c)–(f) Meridional distribution of surface pressure and precipitation for four selected atmospheric carbon emission concentrations and for August and September. The dashed line marks the equator, and the continuous line indicates the beginning of land. For details regarding the offset between the beginning of land and the visible difference between land and ocean refer to Fig. 2.

and for the 1120 ppm setup up to 28°N (Fig. 11b). The number of months with monsoon rainfall are independent of the carbon dioxide concentration (Fig. S16). The strongest increase of monthly rainfall occurs in September and October.

Regarding the Hadley cell, there is a stronger seasonal variation of the ITCZ for higher carbon dioxide concentrations (Fig. S15). This leads to the effect that the land is closer to the convection zone during NH summer and facilitates the ITCZ and monsoon trough to "jump over" to the land in the higher concentration simulations. In August, the meridional surface pressure minimum is shifted northward and becomes less pronounced or vanishes for higher carbon dioxide emissions (Figs. 13c,e). Therefore, the local maximum around the coast is relatively smaller, reducing the surface pressure barrier and enabling southerly winds to transport more moisture toward land. Therefore, the rainfall distribution that is bimodal changes: While for 140 ppm there is a dominant maximum in the tropical ocean and another smaller maximum over land at 15°N, the ocean maximum decreases simultaneously as the land maximum increases. In the 1120 ppm configuration, this leads to the outcome that the maximum over land is dominant and therefore the ITCZ abruptly changes to 15°N. In September, the ITCZ is closer to the coast for all simulations. For higher emission scenarios, the convective zones and accordingly the rainfall maxima fall together with a common strengthened maximum over land at 15°N (Figs. 13d,f).

e. Sensitivity to sulfate aerosols

Sulfate aerosols alter the radiation budget directly by backscattering and absorbing the incoming solar shortwave radiation and indirectly by acting as cloud condensation nuclei. How sulfate aerosols affect monsoon dynamics has only recently begun to be investigated (Li et al. 2016). In our sensitivity study, we vary the sulfate aerosol concentration over land from 10^{-7} to 10^{-4} kg m^{-2}.

As an effect of increasing sulfate aerosol concentrations, the amount of clouds is increasing, strengthening the reflection of solar radiation as expected. The additionally prolonged cloud lifetimes suppress surface temperature globally, but strongest over land (Fig. 14a). While the surface temperatures over land fall rapidly when introducing aerosols by the effect of solar dimming, the sea surface temperatures south over the tropical ocean change much less (Fig. S17). The resulting thermal gradient between ocean and land is therefore decreasing, which has the effect that the moisture transport via meridional surface winds toward the land is decreasing. These processes lead to decreasing rainfall over the monsoon region, at a stronger rate compared to global rainfall.

Furthermore, the entire rainfall distribution is shifted southward in simulations with more sulfate aerosols as an effect of the suppressing of the development of a low pressure and thus convective zone. This is also visible in the position of the ITCZ, particularly during NH summer when the low pressure zone is closer to land and thus the induced atmospheric aerosol (Fig. S18). Additionally, the upper Hadley cell extends less far north as a result of decreasing temperatures over land, while the lower Hadley cell expands less far south during NH summer, but more south from January to April.

The monsoon season is shortened with a later onset and earlier retreat for higher sulfate aerosol concentrations (Fig. S19).

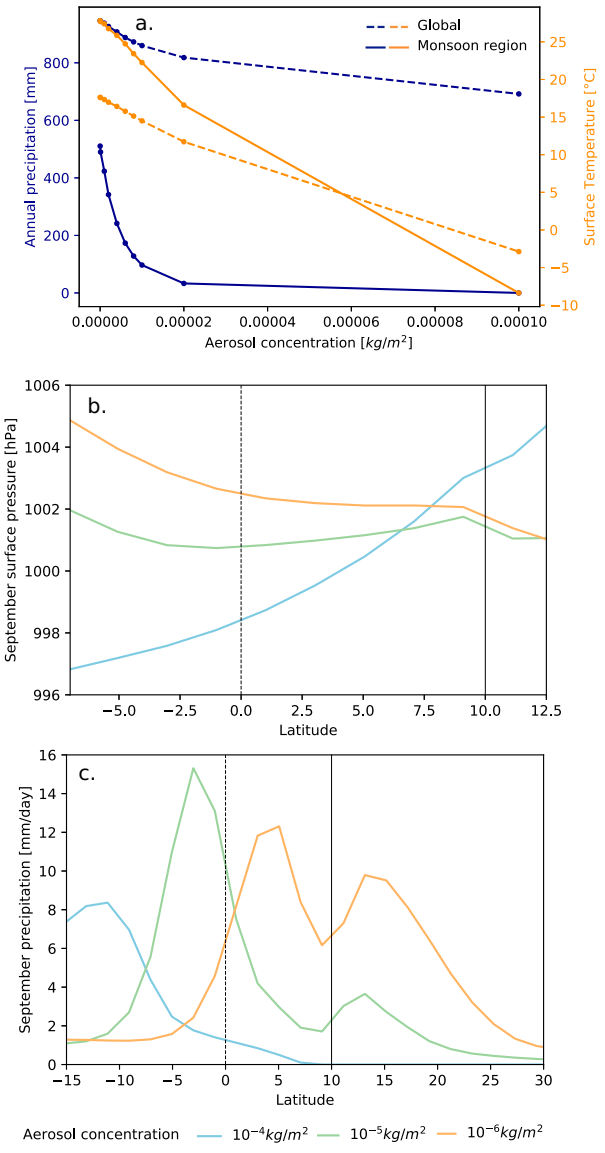

FIG. 14. (a) Sensitivity of precipitation and surface temperature to changes in the sulfate aerosol concentration over land. The continuous lines refer to the relationship in the monsoon region (10°–30°N), while the dashed lines indicate global relationship. (b),(c) Meridional distribution of surface pressure and precipitation for selected solar constant values in September. The dashed line marks the equator and the continuous line indicates the beginning of land. For details regarding the offset between the beginning of land and the visible difference between land and ocean, refer to Fig. 2.

Besides, for an aerosol concentration of 10^{-7} kg m^{-2} the rainfall reaches only up to 27°N, for 10^{-6} kg m^{-2} up to 26°N, for 10^{-5} kg m^{-2} up to 17°N, and for 10^{-4} kg m^{-2} up to 3°S (Fig. 11c).

For simulations with high aerosols, the pressure barrier in September is too high to allow monsoon winds to transport moisture toward north. By reducing the aerosol concentration over land, the relative height of the pressure barrier is reducing enabling moisture transport and thus a bimodal rainfall distribution with monsoon precipitation over land (Figs. 14b,c).

f. *Sensitivity to albedo*

Albedo is the share of reflected incoming sunlight. When the albedo and thus the reflection at the land surface is increased, the share of absorbed radiation that is contributing to the surface temperature is reduced. This has the effect that the surface temperature is going down, too. Here, we are varying the Earth surface albedo over land from 10% to 34%.

As an effect of increased surface albedo, the temperature over land sinks (Fig. 11d). With a smaller slope, the global surface temperatures also decrease, including the area over ocean from 10°S to 10°N (Fig. S20). Therefore, the temperature gradient between land and ocean is reduced, which has the effect that the monsoon winds and accordingly the monsoon rainfall weakens. Simultaneously, the extension of the monsoon area is reduced: while the simulation with a land albedo of 10% expands until 30°N, the 20% albedo run reaches up to 25°N and the 30% albedo setup goes up to 18°N. Besides, the monsoon season onset is shifted from March at the 10% albedo setup to May in the 30% albedo setup. In combination with a retreat one month earlier, the monsoon season is shortened (Fig. S22).

The Hadley cell expands less far north over land for higher land albedo values (Fig. S21) in accordance with the reduced surface temperatures. From May to December, the Hadley cell also expands less south over the ocean. The ITCZ is shifted southward, preventing the effect that the dominant convective zone establishes over land as in the simulations with smaller land albedo.

The pressure barrier dynamic is also present in the albedo simulations in September (Figs. 15b,c): The relative height from the pressure barrier reduces from higher to lower albedo values, letting pass more moisture in low albedo settings. Regarding the monsoon rainfall in dependence of the global mean temperature, the monsoon rainfall reacts quite similarly to GMT changes induced by the solar constant and carbon dioxide on the one hand, as well as sulfate aerosols and albedo on the other hand (Fig. 15d).

5. Discussion

The Monsoon Planet with strong idealization of the land distribution and coupled with a strongly simplified slab ocean is able to replicate major monsoon characteristics reasonably well. Nevertheless, it is important to name the central limitations inherent in this setup: The slab version of an ocean in this study enables us to focus on the atmospheric processes, but at the same time ocean processes are neglected. Besides, zonal dynamics and effects of orography are not considered.

Given the complex interplay between the different climate variables, the question of causality arises. This question is strongly linked to the different response time scales. The time scale for the increase in latent heat due to the condensation during precipitation is on a fast time scale ($\tau_1 \ll 1$ s) as is the direct local temperature increase associated with it. This

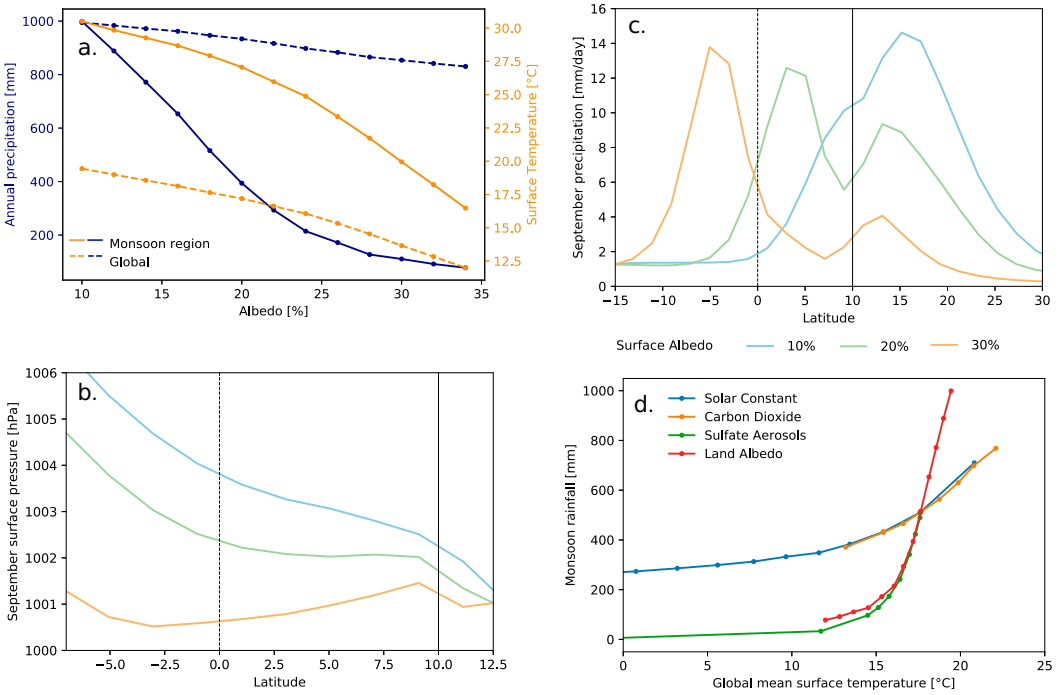

FIG. 15. (a) Sensitivity of precipitation and surface temperature to changes in surface albedo over land. The continuous lines refer to the relationship in the monsoon region (10°–30°N), while the dashed lines indicate global relationship. (b),(c) Meridional distribution of surface pressure and precipitation for three selected albedo simulations in September. The dashed line marks the equator, while the continuous line indicates the beginning of land. (d) The sensitivity of monsoon rainfall to changes in the global mean surface temperature. These surface temperature changes are induced by variation of the slab ocean depth, the solar constant, the atmospheric carbon dioxide concentration, sulfate aerosol concentration, and land albedo.

temperature response is local in the sense that it occurs at the point of condensation. As discussed by Emanuel et al. (1994), this local temperature response is translated into turbulent kinetic energy (i.e., into small-scale turbulent motion and entropy). Thus, the time scale toward a temperature response of the entire atmospheric column is slightly longer (1 min $< \tau_2 <$ 1 h). While the equations within an atmospheric GCM do not resolve the processes on the time scale τ_1 some of the τ_2 processes might be resolved or at least parameterized. The pressure responds quasi-instantaneously to the temperature signal.

The cross-coastal wind field responds to these fast changes with an enhanced transport of moist air toward land, but this process occurs on a much larger time scale ($\tau_3 \gg 1$ h). On the time scale associated with the moisture transport the atmospheric column is in statistical equilibrium. In this sense one might say that the pressure difference is causing the precipitation response. However, since we consider averages over one month or even the entire rainy season, we are averaging over several cycles along the feedback loop. On this long time scale ($\tau_4 = 1$ month) the feedback loop has reached an equilibrium and thus no causality can be claimed. On this time scale, there is also an influence in the other direction.

This issue of causality can be further illustrated by the associated equations that describe the processes. Causality is associated with a prognostic equation while a diagnostic relation between two quantities means that causality cannot be determined. For example, the prognostic equation for the horizontal wind components is able to determine which of the terms (Coriolis term, pressure gradient, etc.) causes a change in the wind field. If, however, we average over a time scale that renders the time derivative of the wind field small, we obtain the geostrophic balance, which is an instantaneous relation between pressure gradient and Coriolis forces. At this level of coarseness, we are not able to determine causality between changes in the wind field and the pressure field.

Since it is the position of the land that we are changing and thereby the radiation over the coast area, we believe that the starting point of the causality loop is the change in the pressure field and the possibility of the development of the pressure barrier. Thus, the causality here is really just caused by the experimental setup, in which we change the position of the land area.

Besides, the authors do not claim that the pressure barrier solely causes the precipitation distribution and therefore has a deterministic character within this mutually consistent dynamic. Another relevant aspect for the rainfall distribution is the water availability in the moisture-providing regions as mentioned.

Pauluis (2004) uses an idealized axisymmetric numerical atmosphere model and focuses on the role of the planetary boundary layer for the cross-equatorial flux. The author finds that the Hadley circulation exhibits two different regimes

depending on the depth of the planetary boundary layer and the sea surface temperature gradient in the equatorial regions associated with the occurrence of the secondary maximum. For a weak temperature gradient or a shallow boundary layer, the return flow is prevented from crossing the equator within the boundary layer and is forced upward to cross the equator in the free troposphere instead. This regime is corresponding to the situation on the Monsoon Planet, when the pressure barrier (which is dependent on the sea surface temperature gradient) is too high and the convection occurs over ocean leading to a dominating rainfall maximum over the ocean. When the sea surface temperature gradient is strong enough, the winds can pass the equator and the coast, and the major convection takes place over land—associated with a stronger monsoon rainfall. This regime is associated with the situation of the Monsoon Planet with a dominating rainfall maximum over the monsoon region. The study of Pauluis (2004) uses prescribed sea surface temperatures that differ from the more realistic surface temperature distributions resulting from the incoming solar radiation in our study. Besides, the land stripe in the Monsoon Planet setup is another step toward a more realistic monsoon setting.

Determining the distribution of precipitation and its interaction with the large-scale flow is an unsolved problem in tropical meteorology (Nie et al. 2010). In recent decades, the approach of a quasi-equilibrium theory of moist convection (Arakawa and Schubert 1974; Emanuel et al. 1994) has emerged. In this framework the peak upper-level temperatures align with the highest near-surface moist entropy, measured in terms of the equivalent potential temperature Θ_e (Boos and Kuang 2010). The ascent zone where also the monsoon rainfall takes place is located just equatorward of these maxima (Emanuel et al. 1994; Privé and Plumb 2007; Nie et al. 2010; Boos and Kuang 2010; Zhou and Xie 2018; Singh et al. 2017). Also, in the idealized Monsoon Planet configurations, the specific location of ascent motion and associated rainfall is not taking place at the surface pressure minimum, but equatorward of the equivalent potential temperature maximum. In combination with the fact that the pressure is located poleward of the pressure barrier, the distribution of monsoon rainfall can be approximated as the region between the pressure barrier and the maximum of equivalent potential temperature.

The effect of the land position on the monsoon precipitation has also been analyzed by Hui and Bordoni (2021) in a similar setup with equatorward coastline of 0°, 10°, 20°, 30°, and 40°N, reaching the conclusion that the rapid migration of the convergence zone over the continent is only possible when land is placed in tropical latitudes (0°, 10°, 20°N). Thus, Hui and Bordoni (2021) also find a range for equatorward coast positions that permits the development of monsoon dynamics, but the upper threshold for this range differs compared to our study (20°N compared to 12°N). This can be explained by the different depth of the mixed ocean layer. The smaller heat capacity in the 20 m slab ocean enables the convergence zone to reach latitudes farther poleward, while the ocean in this study with a depth of 50 m cannot reach thermal equilibrium fast enough before the insolation continues to move away.

Hui and Bordoni (2021) also report bimodality in the meridional rainfall distribution in all of their simulations with most distinct maxima in the 30° and 40°N setup. They analyze the ratio of precipitation due to moisture flux convergence (calculated as $P - E/P$, where P is precipitation and E evaporation). In their 40°N simulation, they report that the fraction never exceeds 20%, indicating a strong influence of local evaporation concluding that the secondary maxima are artifacts of using a fully saturated surface in their model. (In their 10° simulation, the ratio reaches up to 70% during the peak of the summer, indicating dominance of the moisture flux convergence.) In comparison, in our 10° simulation where bimodality is clearly present, the fraction reaches up to 49% in September. In our 2° and 4°N simulations, the moisture flux convergence ratio reaches 58%. Thus, local evaporation does play an important role in our setup, but approximately half or more of the rainfall originates from moisture flux convergence and is regulated by the pressure barrier dynamics. For comparison reasons, note that for example in the Indian monsoon the share of recycled rainfall (originated in local evaporation) is estimated to be between 10% and 40% (Sujith et al. 2017).

A study that also reports a double ITCZ structure and proposes a theoretical framework to explain it is that of Chao (2000). In the study, the author uses numerical experiments with an atmospheric general circulation model over an aquaplanet with zonally uniform SST. Differing from our study, the SST is prescribed and no landmass is implemented. Depending on the specific parameters, a double ITCZ structure evolves which the author explains by two "forces": first, a force that is related to Earth's rotation pulling the ITCZ toward the equator and, second, a force that pulls the ITCZ toward the latitude with the SST peak. This second force is assumed to be relatively linear and varies throughout the year. The location of the ITCZ can then be determined by the stable intersection points. This theory derived from an aquaplanet is not directly transferable because the functional form of the second force is not linear as in Chao (2000), but by the implementation of landmass a second maximum in the surface temperature distribution is added on the Monsoon Planet. Therefore, the functional form will have two minima and the intersection dynamics will be different.

Zhou and Xie (2018) analyzed the sensitivity of monsoon rainfall to changes in albedo on a rectangular-shaped continent and found a linear relationship for a surface albedo between 0.30 and 0.46. While this is a realistic approximation for limited ranges of albedo changes, the perspective of a broader spectrum of albedo values in our study (varying albedo from 0.10 to 0.35) reveals a more general relationship that is not linear. Albedo values larger than 25% basically shut down the idealized monsoon.

Given the idealized character of this study, the question arises if and in which way the pressure–barrier dynamics are influencing real-world monsoon systems. The bimodality of the rainfall distribution that evolves during the course of one year in our idealized setup also emerges in the real-world

West African monsoon region that is shaped most comparably to our stripe setup (rather rectangular continental shape, relatively small influence of orography). The locations of the two rainfall maxima at approximately 6° and 11°N are determined by a barrier in the surface pressure at about 9°N following the structure of the idealized setup on the Monsoon Planet. The relative height of the pressure barrier changes only very little during the season, indicating the relevant role of moisture availability in the moisture supplying areas.

6. Conclusions

In this study, we use the atmospheric model GFDL-AM2 coupled to a slab ocean model in order to simulate a Monsoon Planet setup, namely an aquaplanet with an annulus of land in the Northern Hemisphere. This setup enables us to focus on the meridional monsoon dynamics. We find a pressure barrier regulating the monsoon's intensity that is the focus of this study.

By moving the land stripe from north to south, we identify the land positions that allow monsoon rainfall to develop. For a slab ocean depth of 50 m (chosen in accordance with the mixed ocean layer depth in the real world), these setups include the simulations with equatorward coastlines of 12°N or closer to the equator. We also identify three different possible monsoon dynamics depending on the stripe position: The unimodal monsoon systems (south coast at 0°N), bimodal monsoon systems attracting rainfall (2°, 4°, 6°, 8°, 10°N), and monsoon repellent systems (12°, 14°, 16°N). The rainfall repelling effect in the 12°, 14° and 16°N setups is a result of a local pressure maximum introduced over land shifting the ITCZ and associated rainfall southward. This pressure barrier regulates the monsoon rainfall also for the bimodal monsoon systems.

The slab ocean depth determines the markedness of the seasonal cycle. For a shallower ocean and more intense seasonal cycle, a stronger monsoon develops over land. This is due to the wind directions in the region from 0° to 10°N. For a shallower ocean, the moisture that evaporates in this region is transported northward to the land, whereas in deeper ocean the transport is southward contributing to the equatorial rainfall maximum.

By increasing the solar constant, the global mean temperature increases, leading to enhanced evaporation and increased water vapor in the atmosphere. This in general results in an increase of global precipitation. The variation of the atmospheric carbon dioxide concentration also causes an increase of global temperatures and thermodynamic effects similar to the ones induced by changes in the solar constant. The dependence of monsoon rainfall on global mean temperatures is independent of the origin of the change in global mean temperature. The seasonal variation of the ITCZ is stronger for high carbon dioxide concentrations, reducing the distance between the convection zone and land. Accordingly, the rainfall maximum over the ocean and the rainfall maximum over land become closer until they fall together, cancelling the pressure barrier between the maxima. This is associated with an abrupt change of the dominating rainfall maximum (and thus the ITCZ) from ocean to land as well as a strengthening effect of monsoon rainfall over land.

Sulfate aerosols reduce the planetary albedo with the effect of lower local surface temperatures over land while the tropical sea surface temperatures decrease less strongly. The resulting thermal heat gradient is smaller and therefore the moisture transport via south winds weakens, resulting in less monsoon rainfall. The effect of varying the surface albedo is comparable to the effect of sulfate aerosols.

In conclusion, depending on the parameter set, some simulations produce monsoon dynamics over land, while others do not. The setups with monsoon rainfall reveal a bimodal rainfall distribution with one peak over the tropical ocean and the other one over land. The intensity of the monsoon is regulated by a pressure-barrier dynamic regulating moisture transport toward land. This dynamic is emerging during the course of one year, but also occurs by varying different parameters. Focusing on the monsoon rainfall in dependence of the varied parameter, we do not find an abruptness in these specific relationships. The bimodality in the rainfall distribution during the season is also visible in reanalysis data of the West African monsoon. The locations of the two maxima are determined by a pressure barrier between the two maxima. The concept of the pressure barrier could also be integrated into the understanding of paleoclimate monsoon systems as, for example, in the context of mega-monsoons.

Acknowledgments. The authors gratefully acknowledge the European Regional Development Fund (ERDF), the German Federal Ministry of Education and Research, and Land Brandenburg for supporting this project by providing resources on the high-performance computer system at the Potsdam Institute for Climate Impact Research. This paper is supported within the scope of a GIZ project financed on behalf of the Government of the Federal Republic of Germany under grant agreement 81290341. The research was financially supported by the Heinrich-Boell Foundation, who did not have any influence on the study design, the data analysis, or the interpretation of the results (nor any other influence). This research is also supported by the European Union's Horizon 2020 research and innovation programme under grant agreement 869304.

Data availability statement. All model code used in this study is publicly available. The source code and example datasets for the AM2 atmosphere model, the FMS coupler, and the LaD land model are available via the MOM5 (Griffies et al. 2020) Github repository. The code for the slab ocean model is also available on github (GFDL Team 2019). Model input and output files as well as the scripts used to generate the figures are available at the institutional repository of the Potsdam Institute for Climate Impact Research (https://doi.org/10.5880/PIK.2022.002) (Katzenberger et al. 2022a).

REFERENCES

Almazroui, M., S. Saeed, F. Saeed, M. N. Islam, and M. Ismail, 2020: Projections of precipitation and temperature over the South Asian countries in CMIP6. *Earth Syst. Environ.*, **4**, 297–320, https://doi.org/10.1007/s41748-020-00157-7.

An, Z., and Coauthors, 2015: Global monsoon dynamics and climate change. *Annu. Rev. Earth Planet. Sci.*, **43**, 29–77, https://doi.org/10.1146/annurev-earth-060313-054623.

Anderson, J. L., and Coauthors, 2004: The new GFDL global atmosphere and land model AM2–LM2: Evaluation with prescribed SST simulations. *J. Climate*, **17**, 4641–4673, https://doi.org/10.1175/JCLI-3223.1.

Arakawa, A., and W. H. Schubert, 1974: Interaction of a cumulus cloud ensemble with the large-scale environment, Part I. *J. Atmos. Sci.*, **31**, 674–701, https://doi.org/10.1175/1520-0469(1974)031<0674:IOACCE>2.0.CO;2.

——, and V. R. Lamb, 1977: Computational design of the basic dynamical processes of the UCLA general circulation model. *General Circulation Models of the Atmosphere*, Methods in Computational Physics: Advances in Research and Applications, Vol. 17, Elsevier, 173–265.

Bollasina, M. A., Y. Ming, and V. Ramaswamy, 2011: Anthropogenic aerosols and the weakening of the South Asian summer monsoon. *Science*, **334**, 502–505, https://doi.org/10.1126/science.1204994.

Bony, S., and Coauthors, 2015: Clouds, circulation and climate sensitivity. *Nat. Geosci.*, **8**, 261–268, https://doi.org/10.1038/ngeo2398.

Boos, W. R., and Z. Kuang, 2010: Dominant control of the South Asian monsoon by orographic insulation versus plateau heating. *Nature*, **463**, 218–222, https://doi.org/10.1038/nature08707.

Bordoni, S., and T. Schneider, 2008: Monsoons as eddy-mediated regime transitions of the tropical overturning circulation. *Nat. Geosci.*, **1**, 515–519, https://doi.org/10.1038/ngeo248.

Cai, Y., and Coauthors, 2015: Variability of stalagmite-inferred Indian monsoon precipitation over the past 252,000 y. *Proc. Natl. Acad. Sci. USA*, **112**, 2954–2959, https://doi.org/10.1073/pnas.1424035112.

Chao, W. C., 2000: Multiple quasi equilibria of the ITCZ and the origin of monsoon onset. *J. Atmos. Sci.*, **57**, 641–652, https://doi.org/10.1175/1520-0469(2000)057<0641:MQEOTI>2.0.CO;2.

Chen, Z., T. Zhou, L. Zhang, X. Chen, W. Zhang, and J. Jiang, 2020: Global land monsoon precipitation changes in CMIP6 projections. *Geophys. Res. Lett.*, **47**, e2019GL086902, https://doi.org/10.1029/2019GL086902.

Cherchi, A., A. Alessandri, S. Masina, and A. Navarra, 2011: Effects of increased CO_2 levels on monsoons. *Climate Dyn.*, **37**, 83–101, https://doi.org/10.1007/s00382-010-0801-7.

Chou, C., J. D. Neelin, and H. Su, 2001: Ocean-atmosphere-land feedbacks in an idealized monsoon. *Quart. J. Roy. Meteor. Soc.*, **127**, 1869–1891, https://doi.org/10.1002/qj.49712757602.

Delworth, T. L., and Coauthors, 2006: GFDL's CM2 global coupled climate models. Part I: Formulation and simulation characteristics. *J. Climate*, **19**, 643–674, https://doi.org/10.1175/JCLI3629.1.

Ding, Y., 2007: The variability of the Asian summer monsoon. *J. Meteor. Soc. Japan*, **85B**, 21–54, https://doi.org/10.2151/jmsj.85B.21.

——, Y. Liu, Y. Song, and J. Zhang, 2015: From MONEX to the global monsoon: A review of monsoon system research. *Adv. Atmos. Sci.*, **32**, 10–31, https://doi.org/10.1007/s00376-014-0008-7.

Dirmeyer, P. A., 1998: Land-sea geometry and its effect on monsoon circulations. *J. Geophys. Res.*, **103**, 11 555–11 572, https://doi.org/10.1029/98JD00802.

Emanuel, K. A., J. D. Neelin, and C. S. Bretherton, 1994: On large-scale circulations in convecting atmospheres. *Quart. J. Roy. Meteor. Soc.*, **120**, 1111–1143, https://doi.org/10.1002/qj.49712051902.

GFDL Team, 2019: GFDL FMS Slab Ocean Model. GitHub, accessed 15 January 2024, https://github.com/NOAA-GFDL/SM2.

Griffies, S., and Coauthors, 2020: MOM5 Modular Ocean Model. GitHub, accessed 3 June 2022, https://mom-ocean.github.io/.

Ha, K.-J., S. Moon, A. Timmermann, and D. Kim, 2020: Future changes of summer monsoon characteristics and evaporative demand over Asia in CMIP6 simulations. *Geophys. Res. Lett.*, **47**, e2020GL087492, https://doi.org/10.1029/2020GL087492.

Hadley, G., 1735: VI. Concerning the cause of the general trade-winds. *Philos. Trans. Roy. Soc.*, **39**, 58–62, https://doi.org/10.1098/rstl.1735.0014.

Halley, E., 1686: An historical account of the trade winds, and monsoons, observable in the seas between and near the Tropicks, with an attempt to assign the physical cause of the said winds. *Philos. Trans. Roy. Soc.*, **16**, 153–168, https://doi.org/10.1098/rstl.1686.0026.

Hartmann, D. L., 2016: *Global Physical Climatology*. Vol. 103. 2nd ed. Elsevier, 498 pp.

Hess, P. G., D. S. Battisti, and P. J. Rasch, 1993: Maintenance of the intertropical convergence zones and the large-scale tropical circulation on a water-covered earth. *J. Atmos. Sci.*, **50**, 691–713, https://doi.org/10.1175/1520-0469(1993)050<0691:MOTICZ>2.0.CO;2.

Hu, Y., and Q. Fu, 2007: Observed poleward expansion of the Hadley circulation since 1979. *Atmos. Chem. Phys.*, **7**, 5229–5236, https://doi.org/10.5194/acp-7-5229-2007.

Hui, K. L., and S. Bordoni, 2021: Response of monsoon rainfall to changes in the latitude of the equatorward coastline of a zonally symmetric continent. *J. Atmos. Sci.*, **78**, 1429–1444, https://doi.org/10.1175/JAS-D-20-0110.1.

Johanson, C. M., and Q. Fu, 2009: Hadley cell widening: Model simulations versus observations. *J. Climate*, **22**, 2713–2725, https://doi.org/10.1175/2008JCLI2620.1.

Katzenberger, A., J. Schewe, J. Pongratz, and A. Levermann, 2021: Robust increase of Indian monsoon rainfall and its variability under future warming in CMIP6 models. *Earth Syst. Dyn.*, **12**, 367–386, https://doi.org/10.5194/esd-12-367-2021.

——, A. Levermann, S. Petri, and G. Feulner, 2022a: Monsoon Planet: Simulation data to examine monsoon dynamics with idealized topography. GFZ Data Services, accessed 15 January 2024, https://doi.org/10.5880/PIK.2022.002.

——, ——, J. Schewe, and J. Pongratz, 2022b: Intensification of very wet monsoon seasons in India under global warming. *Geophys. Res. Lett.*, **49**, e2022GL098856, https://doi.org/10.1029/2022GL098856.

Kitoh, A., S. Yukimoto, A. Noda, and T. Motoi, 1997: Simulated changes in the Asian summer monsoon at times of increased atmospheric CO_2. *J. Meteor. Soc. Japan*, **75**, 1019–1031, https://doi.org/10.2151/jmsj1965.75.6_1019.

Knutson, T., 2003: FMS slab ocean model technical documentation. GFDL, accessed 3 June 2022, http://www.gfdl.noaa.gov/fms-slab-ocean-model-technical-documentation.

Kripalani, R., K.-J. Ha, C.-H. Ho, J.-H. Oh, B. Preethi, M. Mujumdar, and A. Prabhu, 2022: Erratic Asian summer monsoon 2020: Covid-19 lockdown initiatives possible cause for

these episodes? *Climate Dyn.*, **59**, 1339–1352, https://doi.org/10.1007/s00382-021-06042-x.

Lange, S., 2019: WFDE5 over land merged with ERA5 over the ocean (W5E5). V. 1.0. GFZ Data Services, accessed 15 January 2024, https://doi.org/10.5880/pik.2019.023.

Lee, J.-Y., and B. Wang, 2014: Future change of global monsoon in the CMIP5. *Climate Dyn.*, **42**, 101–119, https://doi.org/10.1007/s00382-012-1564-0.

Levermann, A., J. Schewe, V. Petoukhov, and H. Held, 2009: Basic mechanism for abrupt monsoon transitions. *Proc. Natl. Acad. Sci. USA*, **106**, 20 572–20 577, https://doi.org/10.1073/pnas.0901414106.

Li, Z., and Coauthors, 2016: Aerosol and monsoon climate interactions over Asia. *Rev. Geophys.*, **54**, 866–929, https://doi.org/10.1002/2015RG000500.

Lobo, A. H., and S. Bordoni, 2020: Atmospheric dynamics in high obliquity planets. *Icarus*, **340**, 113592, https://doi.org/10.1016/j.icarus.2019.113592.

Manabe, S., 1969: Climate and the ocean circulation: I. The atmospheric circulation and the hydrology of the Earth's surface. *Mon. Wea. Rev.*, **97**, 739–774, https://doi.org/10.1175/1520-0493(1969)097<0739:CATOC>2.3.CO;2.

——, 2019: Role of greenhouse gas in climate change. *Tellus*, **71A**, 1620078, https://doi.org/10.1080/16000870.2019.1620078.

Marshall, J., D. Ferreira, J.-M. Campin, and D. Enderton, 2007: Mean climate and variability of the atmosphere and ocean on an aquaplanet. *J. Atmos. Sci.*, **64**, 4270–4286, https://doi.org/10.1175/2007JAS2226.1.

Meehl, G. A., and W. M. Washington, 1993: South Asian summer monsoon variability in a model with doubled atmospheric carbon dioxide concentration. *Science*, **260**, 1101–1104, https://doi.org/10.1126/science.260.5111.1101.

Milly, P. C. D., and A. B. Shmakin, 2002: Global modeling of land water and energy balances. Part I: The Land Dynamics (LaD) model. *J. Hydrometeor.*, **3**, 283–299, https://doi.org/10.1175/1525-7541(2002)003<0283:GMOLWA>2.0.CO;2.

Mohtadi, M., M. Prange, and S. Steinke, 2016: Palaeoclimatic insights into forcing and response of monsoon rainfall. *Nature*, **533**, 191–199, https://doi.org/10.1038/nature17450.

Moon, S., and K.-J. Ha, 2020: Future changes in monsoon duration and precipitation using CMIP6. *npj Climate Atmos. Sci.*, **3**, 45, https://doi.org/10.1038/s41612-020-00151-w.

Nie, J., W. R. Boos, and Z. Kuang, 2010: Observational evaluation of a convective quasi-equilibrium view of monsoons. *J. Climate*, **23**, 4416–4428, https://doi.org/10.1175/2010JCLI3505.1.

Pauluis, O., 2004: Boundary layer dynamics and cross-equatorial Hadley circulation. *J. Atmos. Sci.*, **61**, 1161–1173, https://doi.org/10.1175/1520-0469(2004)061<1161:BLDACH>2.0.CO;2.

Prell, W. L., and J. E. Kutzbach, 1987: Monsoon variability over the past 150,000 years. *J. Geophys. Res.*, **92**, 8411–8425, https://doi.org/10.1029/JD092iD07p08411.

Privé, N. C., and R. A. Plumb, 2007: Monsoon dynamics with interactive forcing. Part I: Axisymmetric studies. *J. Atmos. Sci.*, **64**, 1417–1430, https://doi.org/10.1175/JAS3916.1.

Ramage, C. S., 1971: *Monsoon Meteorology*. Academic Press, 296 pp.

Sarangi, C., V. P. Kanawade, S. N. Tripathi, A. Thomas, and D. Ganguly, 2018: Aerosol-induced intensification of cooling effect of clouds during Indian summer monsoon. *Nat. Commun.*, **9**, 9754, https://doi.org/10.1038/s41467-018-06015-5.

Seth, A., A. Giannini, M. Rojas, S. A. Rauscher, S. Bordoni, D. Singh, and S. J. Camargo, 2019: Monsoon responses to climate changes—Connecting past, present and future. *Curr. Climate Change Rep.*, **5**, 63–79, https://doi.org/10.1007/s40641-019-00125-y.

Singh, M. S., Z. Kuang, and Y. Tian, 2017: Eddy influences on the strength of the Hadley circulation: Dynamic and thermodynamic perspectives. *J. Atmos. Sci.*, **74**, 467–486, https://doi.org/10.1175/JAS-D-16-0238.1.

Smith, R. S., C. Dubois, and J. Marotzke, 2006: Global climate and ocean circulation on an aquaplanet ocean–atmosphere general circulation model. *J. Climate*, **19**, 4719–4737, https://doi.org/10.1175/JCLI3874.1.

Sujith, K., S. K. Saha, S. Pokhrel, A. Hazra, and H. S. Chaudhari, 2017: The dominant modes of recycled monsoon rainfall over India. *J. Hydrometeor.*, **18**, 2647–2657, https://doi.org/10.1175/JHM-D-17-0082.1.

Voigt, A., and Coauthors, 2016: The Tropical Rain belts with an Annual Cycle and a Continent Model Intercomparison project: TRACMIP. *J. Adv. Model. Earth Syst.*, **8**, 1868–1891, https://doi.org/10.1002/2016MS000748.

Wang, B., and Q. Ding, 2008: Global monsoon: Dominant mode of annual variation in the tropics. *Dyn. Atmos. Oceans*, **44**, 165–183, https://doi.org/10.1016/j.dynatmoce.2007.05.002.

——, C. Jin, and J. Liu, 2020: Understanding future change of global monsoons projected by CMIP6 models. *J. Climate*, **33**, 6471–6489, https://doi.org/10.1175/JCLI-D-19-0993.1.

Wang, Y., and Coauthors, 2008: Millennial- and orbital-scale changes in the East Asian monsoon over the past 224,000 years. *Nature*, **451**, 1090–1093, https://doi.org/10.1038/nature06692.

Winton, M., 2000: A reformulated three-layer sea ice model. *J. Atmos. Oceanic Technol.*, **17**, 525–531, https://doi.org/10.1175/1520-0426(2000)017<0525:ARTLSI>2.0.CO;2.

Xie, S.-P., and N. Saiki, 1999: Abrupt onset and slow seasonal evolution of summer monsoon in an idealized GCM simulation. *J. Meteor. Soc. Japan*, **77**, 949–968, https://doi.org/10.2151/jmsj1965.77.4_949.

Zhao, Z.-C., and W. W. Kellogg, 1988: Sensitivity of soil moisture to doubling of carbon dioxide in climate model experiments. Part II: The Asian monsoon region. *J. Climate*, **1**, 367–378, https://doi.org/10.1175/1520-0442(1988)001<0367:SOSMTD>2.0.CO;2.

Zhou, T., R. Yu, H. Li, and B. Wang, 2008: Ocean forcing to changes in global monsoon precipitation over the recent half-century. *J. Climate*, **21**, 3833–3852, https://doi.org/10.1175/2008JCLI2067.1.

Zhou, W., and S.-P. Xie, 2018: A hierarchy of idealized monsoons in an intermediate GCM. *J. Climate*, **31**, 9021–9036, https://doi.org/10.1175/JCLI-D-18-0084.1.